Coastal Engineering 177 (2022) 104172

Contents lists available at ScienceDirect

Coastal Engineering

journal homepage: www.elsevier.com/locate/coastaleng

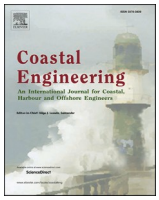

Analysis of the mechanics of breaker bar generation in cross-shore beach profiles based on numerical modelling

J. García-Maribona, J.L. Lara *, M. Maza, I.J. Losada

IHCantabria - Instituto de Hidráulica Ambiental de La Universidad de Cantabria, Isabel Torres 15, 39011, Santander, Spain

A B S T R A C T

In this work, a recently developed numerical model, capable of solving the hydro- and morphodynamics of the cross-shore beach profile, is used to gain insight into the relevant processes driving the generation of a breaker bar. The bedload and suspended sediment transport contributions are analysed separately. It has been shown that the bedload transport tends to accumulate sediment on the onshore side of the undertow detachment point, at a distance that depends on the skewness of the waves and the magnitude of the friction velocity, shaping the onshore face of the breaker bar. In contrast, the suspended transport contributes to the growth of the offshore side of the breaker bar. Besides, a comparison between the sediment transport rates produced by different types of breakers shows a faster bathymetric evolution and an offshore displacement of the position of the breaker bar for high Iribarren numbers. Differences are consistent with the proposed mechanisms driving the evolution of the beach profile. The findings of this work provide a better understanding of the processes driving the formation of breaker bars, how they interact with each other and the relative importance of bedload and suspended sediment transport at each location of the cross-shore profile.

1. Introduction

The mechanisms governing the interaction between hydrodynamics, sediment transport and bathymetry changes that occurs in cross-shore beach profiles during episodic events are still not fully understood. The limitations of laboratory techniques associated with mobile bed conditions (such as scaling effects) and the simultaneous measurement of fluid and sediment related variables with high spatial and temporal resolution hinder the understanding of the processes that drive beach profile evolution. Field measurements also encounter several difficulties when gathering detailed observations, especially under highly energetic wave conditions, such as ensuring the survivability and correct functioning of the instruments or finding the time windows to measure under the desired environmental conditions. As a result, the evolution of beach profiles is generally explained in an oversimplified manner, leading to important limitations. Among them, predictive models commonly used to assess coastal erosion have to rely on several calibration parameters, limiting their accuracy and predicting skills. Consequently, a deeper understanding on the effect of the hydrodynamics-sediment transport interaction on cross-shore beach profile evolution is needed.

Cross-shore beach profile hydrodynamics has been a research topic for a long time. Some of the hydrodynamic processes tightly related to sediment transport, as indicated in (Svendsen, 2006), are the generation of the undertow in the surf zone, the steady streaming due to progressive waves, the velocity and acceleration skewness due to wave skewness and asymmetry and the wave breaking process.

The undertow was observed for the first time in a laboratory experiment by (Bagnold, 1940). In (Longuet-Higgins, 1983), it was found that the near-bed mean flow is directed offshore in the surf zone due to its effect, changing its direction before reaching the break point. The location at which the near-bed current changes its direction was named undertow detachment point. Later (Deigaard et al., 1991), developed a model to predict the undertow velocity profile accounting for different sources of stresses in the fluid, arising from the radiation stress gradient, effects of surface rollers, steady streaming and the variation of the mean water level. More experiments have been conducted to investigate the undertow velocity profile, and different models based on experimental and field measurements have been developed aiming to quantify it (e.g. (Rattanapitikon and Shibayama, 2000), or (Garcez Faria et al., 2000)).

The steady streaming produced by waves, which results in a near-bed current, was addressed by (Longuet-Higgins and Stoneley, 1953) and, more recently, by (Holmedal & Myrhaug, 2009) and (Blondeaux et al., 2012). All these studies were performed in a flat bed. They found that the total steady streaming is a combination of two competing mechanisms: the first one due to the near-bed vertical velocities generated by waves, and the second due to the differences in near-bed turbulent viscosity during the wave crest and trough phases that arise from wave skewness. In the case of a cross-shore beach profile, the influence of the sloped seabed, wave breaking, and the effect of mass flux produced by

* Corresponding author.
E-mail address: lopezjav@unican.es (J.L. Lara).

https://doi.org/10.1016/j.coastaleng.2022.104172
Received 15 November 2021; Received in revised form 16 June 2022; Accepted 1 July 2022
Available online 9 July 2022

the undertow add extra complexity to the analysis of the steady streaming. The near-bed velocity and acceleration skewness that result from the wave skewness and asymmetry can induce sediment transport *per-se* as discussed by (van Rijn et al., 2013).

Finally, the wave breaking process has been extensively studied as it greatly influences the hydrodynamics in the surf zone. The mass and momentum flux unbalances arising from it are responsible for the generation of the undertow and wave set-up (Svendsen, 1984). A key aspect regarding wave breaking is the influence that the vortices and turbulence resulting from it have on the undertow, as discussed by (Ting and Nelson, 2011). (Ting and Kirby, 1995) and (Ting and Kirby, 1994) presented the differences in the turbulence produced by plunging and spilling breakers and its effect in the momentum exchange between the upper and lower layers of the surf zone. More recently (van der A et al., 2017), measured the velocities generated during wave breaking and the production and transport of TKE. Other recent studies on wave breaking are based on detailed numerical models instead of laboratory experiments. For instance (Lubin et al., 2006) used a LES model to provide insight into the breaking process, and (Larsen et al., 2020) simulated waves breaking over a bar to obtain detailed hydrodynamic data on relevant processes (e.g. undertow velocities, turbulence, etc.) using a RANS model.

The sediment transport mechanisms produced by such complex hydrodynamic effects have been also widely studied. In the shoaling zone, our understanding of the bedload and suspended transport mechanisms has improved during the last years as explained by (van Rijn et al., 2013). In the surf zone, more recent studies have also provided more insight into the way in which wave breaking and undertow influence the sediment transport. Regarding the shoaling zone, the main hydrodynamic mechanisms influencing sediment transport are steady streaming and wave skewness. The importance of steady streaming in sediment transport was highlighted by (Longuet-Higgins and Stoneley, 1953). The effects of velocity and acceleration skewness on the prediction of sediment transport rates was addressed by (Ruessink et al., 2011). In the surf zone, the undertow is a key aspect influencing sediment transport, as stated by (Gallagher et al., 1998). Additionally, the complex hydrodynamic conditions resulting from wave breaking (such as turbulence production, generation of coherent structures or air entrainment among others) greatly affect the bedload and suspended transport mechanisms. Concerning the suspended transport (Sumer et al., 2013), presented how the shear stress induced by breaking waves can result in a large amount of sediment put into suspension. Also, the turbulence produced during wave breaking has a fundamental role in keeping sediment in suspension inside the surf zone, as discussed by (Ting and Kirby, 1995). This was also observed in a natural beach by (Aagard and Jensen, 2013) and, more recently, it was experimentally and numerically studied in (van der Zanden et al., 2017a) and using a LES model by (Otsuka et al., 2017), respectively. Regarding the bedload transport, the influence of the wave breaking process was addressed by (van der Zanden et al., 2017b).

The bathymetric evolution of the beach profile, resulting from sediment transport induced by nearshore hydrodynamics, has been traditionally related to wave conditions (*H, T, h*) and sediment characteristics. Due to their simplicity, some of the early models developed in this way (e.g. (Bruun, 1954), (Dean, 1977)) are still widely used in several coastal engineering applications to estimate the shape of the beach profile once equilibrium conditions are reached. This approach, directly relating incident wave conditions to the resulting equilibrium profile, is being used in more recent studies to account for important morphological features such as breaker bars, which are not accounted for in previous models. For example (Baldock et al., 2011), studied the relationship between different incident wave conditions, including irregular waves and bathymetric changes. In (Caceres and Alsina, 2016) related the incident wave conditions to the breaker bar dimensions. Also, in (Ruessink et al., 2009) the influence of wave climate in the migration of the breaker bars in a double-barred profile is studied based on field data. However, these approaches do not include explicitly the hydrodynamic and sediment transport features, nor the changes that bathymetric evolution may induce on them.

Despite the significant advancements in the understanding of hydrodynamics – sediment transport interactions, the current knowledge on how they relate to the evolution of the bathymetry is still not enough to provide reliable predictions, and models based on this approach require the use of several calibration parameters to compensate this knowledge gap (e.g. (Kalligeris et al., 2020), (Ruffini et al., 2020)). A global approach that integrates the existing knowledge on morphodynamic processes involved in the cross-shore beach profile evolution and the interactions between them is required to understand how they drive its evolution. The previous work from (Walstra, 2016) shows that better understanding of the morphodynamic processes has great potential for improving numerical predictions.

In this work, the underlying physical processes leading to the generation of a breaker bar in a beach profile are studied in conjunction. The main objective is to explain how different components of the hydrodynamics-sediment transport interaction influence the generation of a breaker bar. The analysis is based on data obtained from a newly developed numerical model coupling a RANS hydrodynamic model and a sediment transport module. The methodology used for this analysis is presented in Section (2). The results of the analysis are given and discussed in Section (3). Finally, the main conclusions are given in Section (4).

2. Methodology

2.1. Description of the numerical model

The in-depth analysis of the interactions between hydrodynamics, sediment transport and bathymetric changes in the cross-shore profile is based on the numerical simulation of a study case, performed with the 2D RANS Eulerian One-phase model IH2VOF-SED (García-Maribona et al., 2021). The model consists of two main modules solving the hydrodynamics and sediment transport which are two-way coupled.

The hydrodynamic module solves the 2D RANS equations, which are derived from the mass and momentum conservation equations. A $k-\varepsilon$ turbulence model is included to account for the effect of turbulent motions. In order to track the position of the free surface, the Volume of Fluid (VoF) method is used. The effect of solid boundaries is included by using a partial cell treatment. A method based on the interpolation of the velocity field to a set of points at a constant distance from the wall is applied to better approximate the friction velocity of the boundary layer, mitigating the numerical errors close to solid surfaces inherent to the use of the partial cell technique. The hydrodynamic model has been previously validated and used in different studies. In (Torres-Freyermuth et al., 2007) the model was used to reproduce hydrodynamic processes in the surf zone, comparing numerical results with experimental data of bottom pressure, wave height, breaking index, velocities, energy and momentum fluxes. Also, in (Lara et al., 2006), the hydrodynamic model was used to study irregular wave interaction with submerged permeable breakwaters, including a comparison of the results with experimental data from laboratory tests.

Regarding the sediment transport, the bedload and suspended mechanisms are solved following different strategies. For the bedload transport, the methodology from (Roulund et al., 2005), which uses the empirical formulae from (Engelund and Fredsoe, 1976) (eq. (1)), is selected.

$$q_{bl} = \frac{1}{6} d_{50} P_{ef} U_p \tag{1}$$

In which q_{bl} is the bedload transport, d_{50} is the nominal grain diameter, P_{ef} is the proportion of moving particles on the seabed and U_p the velocity at which the particles move. Both P_{ef} and U_p vary in time, as they depend on the instantaneous friction velocity.

The suspended transport contribution is calculated by solving an

advective-diffusive transport equation for the sediment concentration. The transition of sediment into suspension is modelled with a boundary condition on the seabed that depends on the concentration gradient on the seabed. To obtain it, the reference concentration formula from (Smith and McLean, 1977) is used. The friction velocity on the seabed, needed to compute both transport mechanisms, is obtained from the near-bed velocities by assuming a logarithmic boundary layer profile. Once the sediment transport is computed, a sediment balance is performed for each segment of the seabed to determine the total change in seabed position. The partial cell parameters are then updated so that the hydrodynamic model considers the new position of the seabed in the next time-step. The effect of the seabed slope is accounted for by modifying the critical Shields number of the sediment. A detailed description and validation of the model can be found in (García-Maribona et al., 2021), including the evolution of beach profiles under erosive conditions at different scales and an analysis of the main variables along the cross-shore profile (wave height, tangential stress, and velocity and concentration profiles).

There are some limitations in the use of RANS numerical models related to the time scales of the various processes involved in coastal hydrodynamics. Firstly, there are processes with temporal scales larger than the wave period ($T > T_w$), this is the case of currents such as the undertow and the steady streaming. Secondly, processes with a time-scale similar to that of the wave period ($T \sim T_w$), known as intra-wave variations, such as the changes in flow velocity and sediment concentration along the wave phase. Finally, there are other processes with a time scale smaller than the wave period ($T < T_w$), like turbulent fluctuations produced by breaking waves. In this work, the two first time scales are addressed while the latter one is not considered, as RANS models do not resolve the turbulent fluctuations, but rather consider their effect via a turbulence closure model on the other scales. Additionally, as the numerical model used in this work is two-dimensional, processes such as rip currents, longshore variability or 3D effects of wave breaking are not accounted for.

Although numerical modelling requires introducing certain simplifications of the real phenomena, RANS models do not rely on calibrations and need a reduced number of assumptions to tackle the relevant processes in surf zone hydrodynamics as compared with other standard approaches. These models solve the hydrodynamic processes (i.e., wave breaking or the generation of undertow) based on the RANS equations. They offer the right balance between relevant physical processes simulated, accuracy and required computational effort. Furthermore, the particular model used in this work has been already validated against laboratory data for the evolution of the cross-shore beach profile under erosive conditions in (García-Maribona et al., 2021). Therefore, despite a certain level of empiricism in the sediment transport equations, the results obtained with the numerical model can be considered suitable for the analysis of the underlying phenomena and can contribute to complete potential efforts based on observations. In addition, data and knowledge currently available in the literature are used to back up the numerical results and the conclusions deriving from them.

2.2. Case set-up

The study case is based on the experiments from (Baldock et al., 2011), already modelled with IH2VOF-SED in (García-Maribona et al., 2021) resulting in a good agreement between numerical and experimental results (Brier Skill Score 0.75). Regular wave conditions were used with wave height (H) equal to 43 cm and a wave period (T) of 3.7 s over a water depth (h) at the wave paddle equal to 2.50 m. The nominal diameter of the sediment (d_{50}) was 0.25 mm, and the slope of the initial beach profile was 1:15 approximately.

The numerical domain is designed in accordance with the experimental set-up. It is 41 m long and 2.58 m high. The initial profile has a fully plain 1:15 slope, as this simplifies the analysis of the fundamental processes compared to an irregular initial profile. It starts at 5.82 m from the wave generation boundary in order to accommodate the waves to the water depth before reaching the slope. Regular waves with the same height and period as the experimental set up are generated on the left boundary, at which the water depth is 2.00 m, using Stokes II theory and active wave absorption. The sediment diameter is set to 0.25 mm consistently with the experimental value. The bulk density of the sediment is assumed to be of 2 650 $\frac{kg}{m^3}$ and the sediment porosity equal to 0.40. The computational mesh consists of 146,608 cells (1078x136) with a constant spatial discretization of $\Delta x = 0.038$ m and $\Delta z = 0.019$ m in the horizontal and vertical directions, respectively. A total of 800 waves (2 960 s) are simulated to achieve the equilibrium profile without using any morphological acceleration factor. The simulation took approximately 109 h (4.5 days) running in a single Intel i7-7700K CPU core. The parameters of the model are set as in (García-Maribona et al., 2021), without performing any calibration. The non-dimensional numbers characterizing the beach profile evolution, i.e.: the Iribarren number (Ir_0), Dean parameter (Ω), Rouse number (P) and Shields number (φ), are given in Table 1 and are calculated according to equations eq. (2) to eq. (5).

Table 1
Non-dimensional parameters characterizing the beach profile.

Parameter	Ir_0	Ω	P	φ
Value	0.47	3.42	3.1	0.14

$$Ir_0 = \frac{\tan\alpha}{\sqrt{\frac{H}{L_0}}} \quad (2)$$

$$\Omega = \frac{H}{\omega_s T} \quad (3)$$

$$P = \frac{\omega_s}{u'} \quad (4)$$

$$\varphi = \frac{1}{2} f_\omega \frac{(A\,\omega)^2}{g\left(\frac{\rho_s}{\rho} - 1\right) d_{50}} \quad (5)$$

where α is the slope of the initial beach profile, H is the wave height at the numerical wave paddle, L_0 is the wave length in deep water, ω_s is the sediment fall velocity, T is the wave period, u' is the turbulent fluctuation of the velocity, f_ω is the friction factor, A is the wave stroke close to the seabed, ρ and ρ_s are the water and solid bulk densities, and ω is the angular frequency.

A schematic description of the set-up is given in Fig. 1.

According to the Iribarren number, spilling breakers are expected for the initial configuration ($Ir_0 < 0.50$). However, as it is very close to the spilling breakers limit, the generation of the breaker bar is likely to increase the slope at the breaking point, leading to plunging breakers. Regarding the beach profile, Ω indicates an intermediate state in which a breaker bar is generated. Furthermore, the relatively large scale of this configuration along with the use of natural sand provides realistic conditions that can be expected in nature. Therefore, the configuration of the study case is considered to be adequate for the investigation of the processes leading to the generation of a breaker bar in a cross-shore beach profile.

In the coordinate system used in the following, Z refers to as the vertical distance from the still water level and X to as the horizontal distance from the numerical wave-maker, as shown in Fig. 1. For the discussion of the results, the horizontal coordinate is normalized with the initial wave breaking point position, X_b, and the water depth at that point, h_b (X_b = 27.01 m, h_b = 0.745 m). The breaking point is considered as the position at which the wave height starts decreasing after shoaling. The non-dimensional horizontal coordinate ($\widetilde{x}$) is obtained as:

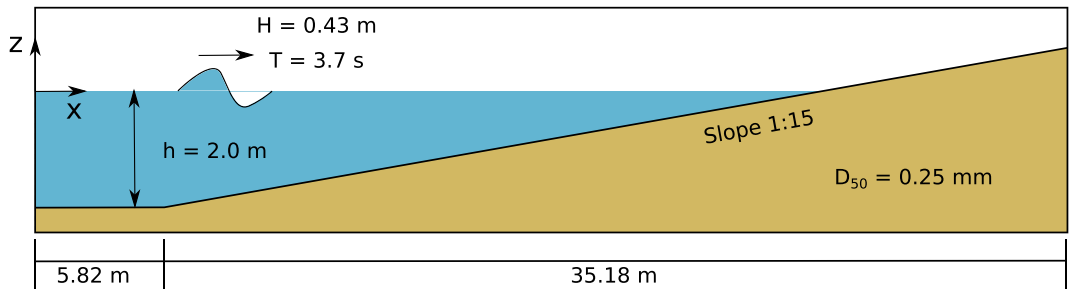

Fig. 1. Schematic description of the numerical set-up (not at scale).

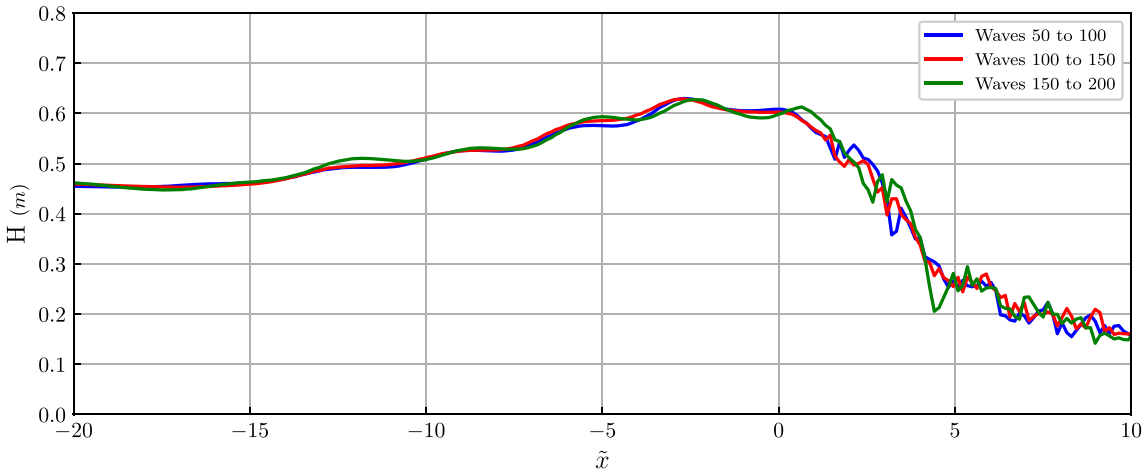

Fig. 2. Distribution of wave height along the cross-shore profile for the first waves of the simulation. Blue line, waves 50 to 100. Red line, waves 100 to 150. Green line, waves 150 to 200.

$$\tilde{x} = \frac{X - X_b}{h_b} \quad (6)$$

In this case, X_b and h_b are obtained considering the breaking point position for the first 150 waves. Fig. 2 shows the time-averaged wave height evolution along the cross-shore profile for the first 200 waves, in 50 waves intervals. The time-averaged wave height for each interval is obtained as the difference between the maximum and minimum of the phase-averaged free surface position. As can be noted, the drop in wave height associated with wave breaking occurs at the nondimensional position $\tilde{x} = 0$. Additionally, the plunge point can be identified approximately at $\tilde{x} = 5$, where the drop in wave height stops with a small increase in wave height due to the water mass displaced by the impinging jet.

Note that, since this is a 2D analysis, the volumetric fluxes of sediment are given per meter of domain width ($\frac{m^3}{s.m}$).

2.3. Identification of the stages of beach profile evolution

For this analysis, the evolution of the beach profile in an extreme event (considered as the occurrence of highly energetic conditions

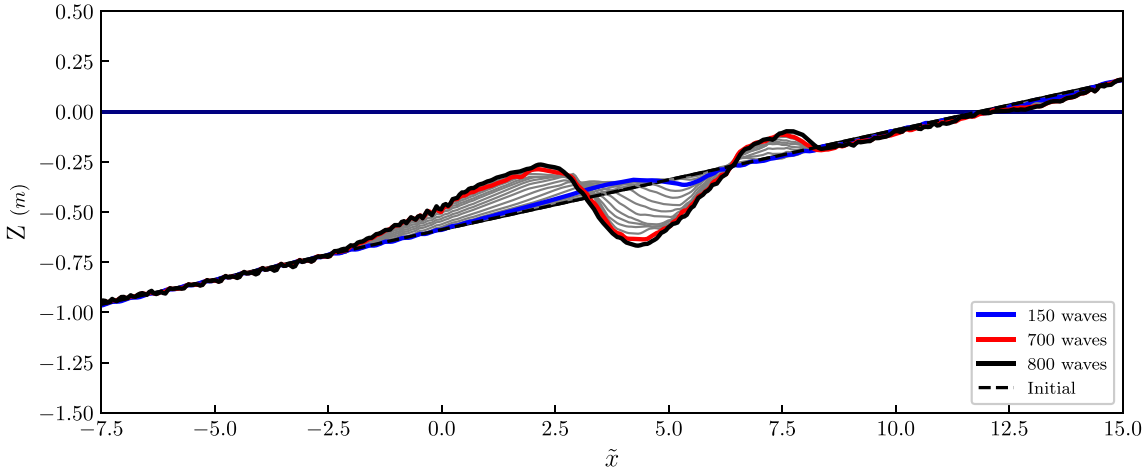

Fig. 3. Bathymetry evolution along the simulation. Black dashed line: initial profile. Blue line: end of the growth stage. Red line: end of the migration stage. Black line: equilibrium profile. Gray lines: intermediate profiles, every 50 waves.

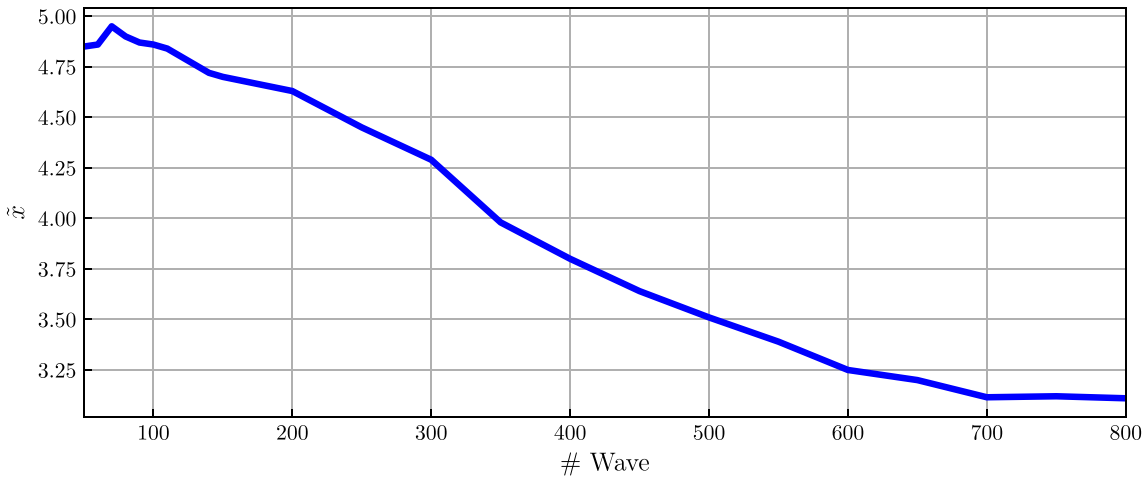

Fig. 4. Evolution of the position of the onshore face of the breaker bar. Obtained as the intersection between the initial profile and the onshore face of the breaker bar at different time steps along the simulation.

leading to significant changes of the cross-shore profile in relatively short periods of time) is conceptualized in three stages attending to the displacement of the breaker bar. Firstly, in the growth stage the breaker bar increases in size while maintaining its position. Then, in the migration stage the breaker bar starts displacing offshore while it keeps increasing its size. Finally, in the equilibrium stage the breaker bar stops displacing and maintains its size if the wave conditions do not change; this stage is only achieved if the duration of the event is large enough.

The first step in this analysis of the results is to identify the aforementioned stages for the study case. For this purpose, the seabed shapes obtained every 50 waves during the simulation are represented in Fig. 3.

As can be noted in Fig. 3, at the beginning of the simulation (first 200 waves) the height of the breaker bar increases nearly maintaining its position. From waves 200 to 700, the bar keeps growing, and the front of the bar starts migrating offshore. After 700 waves, the migration of the bar front stops and the breaker bar is close to its equilibrium status. Sediment is still being accumulated in the offshore face, at a reducing rate, and the height of the breaker bar crest remains constant. Notice that, even though the bar front migrates offshore, the toe of the bar (on the offshore side) does not move significantly after the first 200 waves.

To establish a qualitative criterion for the identification of the bar growth, migration and equilibrium stages in this study case, the position of the onshore face of the breaker bar along the simulation, considered as the intersection between the onshore-facing slope at a certain time and the initial profile, is used as a reference. Its evolution is represented in Fig. 4.

During the first waves of the simulation, initial transient effects associated with the initiation of the hydrodynamic conditions (roughly for the first 50 waves) take place. Due to these transient effects, the position of the onshore face of the breaker bar is displaced onshore, and then, approximately after the next 50 waves, it moves back roughly to the same initial position, as can be observed in Fig. 4. Therefore, the initial transient effects for the hydrodynamics and bathymetry are damped out after the first 100 waves, approximately. It can also be noted that the wave height does not suffer important variations from waves 50 to 100 to waves 100 to 150 (see Fig. 2), showing that the wave conditions are stabilized. After 200 waves, the speed at which the breaker bar migrates starts to increase, indicating the initiation of the migration stage. Considering these aspects, the growth stage is identified in the first 200 waves. The migration stage can be identified in Fig. 4 from waves 200 to 700, and the equilibrium stage from 700 in advance. There are still some bathymetric changes in the last 100 waves of the simulation but, at the end of the equilibrium step, these variations are significantly smaller than the ones of the migration step.

In the following sections, the growth stage is analysed. It is intended to analyse the fundamental processes involved in the generation of a breaker bar, as a first step in the detailed description of the complete evolution of the cross-shore beach profile (including the migration and equilibrium stages). First, the accumulation or loss of sediment in the seabed that led to the bathymetric changes (differentiating the bedload and suspended contributions) is analysed. The sediment transport processes that cause such accumulations or losses are examined next. Finally, the hydrodynamic processes involved in each of the different mechanisms (time-averaged velocity field, vertical time-averaged velocity profiles and friction velocity) are investigated. For this assessment, the wave interval 100 to 150 is considered, as the hydrodynamics and sediment transport can be considered to have reached stabilization, and it is representative of the growth stage (identified for waves 0 to 200).

3. Results

In this section, it is aimed to determine the reasons behind the generation of the breaker bar. For this purpose, the contribution of the two sediment transport mechanisms (suspended and bedload) must be examined separately. Each transport mechanism leads to a particular pattern of accumulation and loss of sediment along the cross-shore profile. These two patterns are responsible for the bathymetric changes. The two rates of accumulation or loss of sediment for each portion of the seabed, which represent the volume of sediment that is being accumulated or lost per unit of time inside it, are calculated as the divergence of the bedload transport (eq. (7)) and the difference between deposition and erosion rates (eq. (8)).

$$\left(\frac{\partial Vol}{\partial t}\right)_{bl} = \nabla\cdot\left(\overrightarrow{Q_{bl}}\right) \tag{7}$$

$$\left(\frac{\partial Vol}{\partial t}\right)_{s} = \vec{D} - \vec{E} \tag{8}$$

where $\left(\frac{\partial Vol}{\partial t}\right)_{bl}$ and $\left(\frac{\partial Vol}{\partial t}\right)_{s}$ are the rate of accumulation or loss of sediment volume in a given portion of the seabed produced by the bedload and suspended mechanisms respectively, $\overrightarrow{Q_{bl}}$ is the bedload transport, and $\vec{E}$ and $\vec{D}$ are the erosion and deposition rates, obtained as the diffusive and advective fluxes of sediment across the seabed boundary. The total rate of accumulation $\left(\frac{\partial Vol}{\partial t}\right)_{t}$ is calculated by adding the two contributions. More information on how these variables are computed can be found in (García-Maribona et al., 2021). The time-averaged rate of accumulation/loss of sediment along the beach profile produced by each

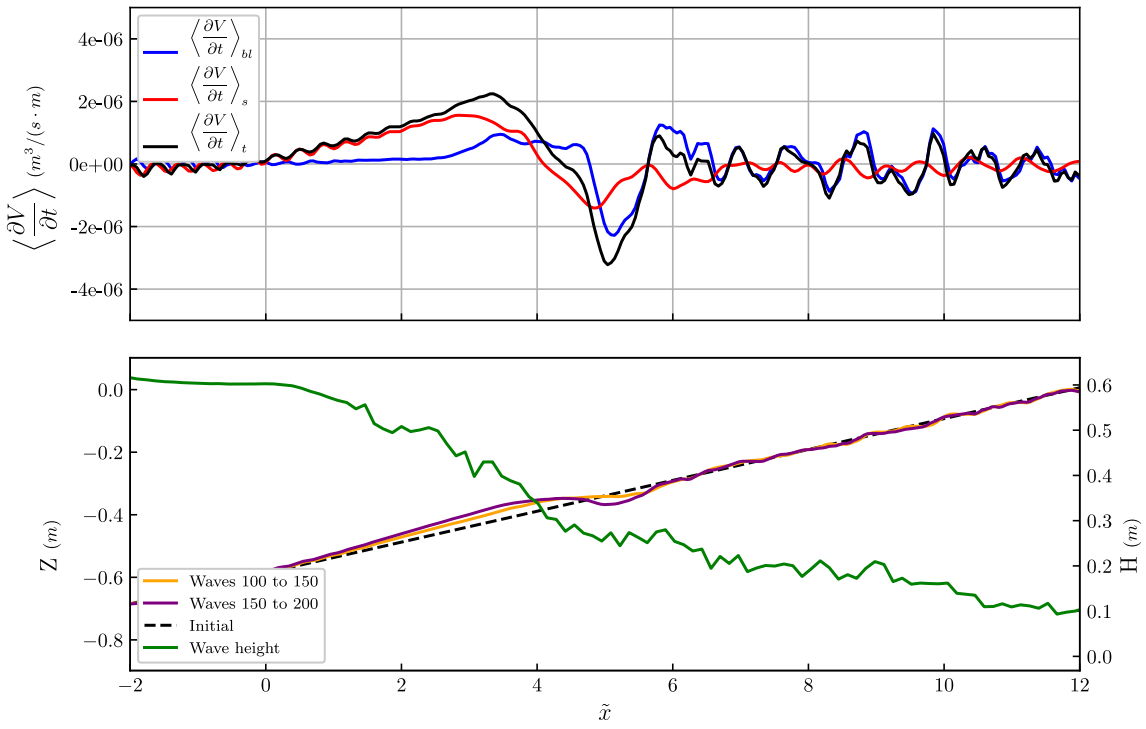

Fig. 5. Top panel (A), time-averaged bedload and suspended accumulation rates for waves 100 to 150. Bottom panel (B), seabed position after 100 and 150 waves.

mechanism, obtained for waves 100 to 150, is depicted in Fig. 5A.

As can be noted, the evolution of the bathymetry in Fig. 5B follows the accumulation/loss rates shown in Fig. 5A, generating the breaker bar in the outer surf zone and a trough at the beginning of the inner surf zone, around the plunge point ($\tilde{x} = 5$). Both suspended and bedload transport tend to accumulate sediment in the outer surf zone (considered as $\tilde{x} = 0$ to $\tilde{x} = 5$), eroding sediment mainly from the inner surf zone ($\tilde{x} > 5$) and, in less amount, from the shoaling zone ($\tilde{x} < 0$). However, there are differences in the accumulation patterns of each contribution. The suspended transport tends to accumulate sediment along most of the outer surf zone ($\tilde{x} = 0$ to $\tilde{x} = 4$), while the bedload transport accumulates sediment just on the onshore side of it ($\tilde{x} = 3$ to $\tilde{x} = 4.5$). This shows that the bedload contribution is the main responsible for the generation of the crest of the breaker bar (onshore face) and the suspended contribution is more relevant for the growth of the tail of the breaker bar (offshore face).

Different approaches have been used to explain these sediment transport mechanisms. Generally, the accumulation of sediment that leads to the generation of the breaker bar is associated with the convergence of an onshore and an offshore sediment transports (Fredsoe and Deigaard, 1992), commonly related to the skewness and asymmetry of shoaling waves and to the influence of the undertow in the surf zone, respectively (Hoefel and Elgar, 2003), (Henderson et al., 2004), (Dubarbier et al., 2015). However, the processes driving the patterns of accumulation or loss of sediment are more complicated. Understanding such processes and the factors that can produce changes in them is fundamental in order to predict the bathymetric variations of a beach profile accurately. In the next sections, the bedload and suspended contributions are analysed separately to gain more insight in the processes that drive them.

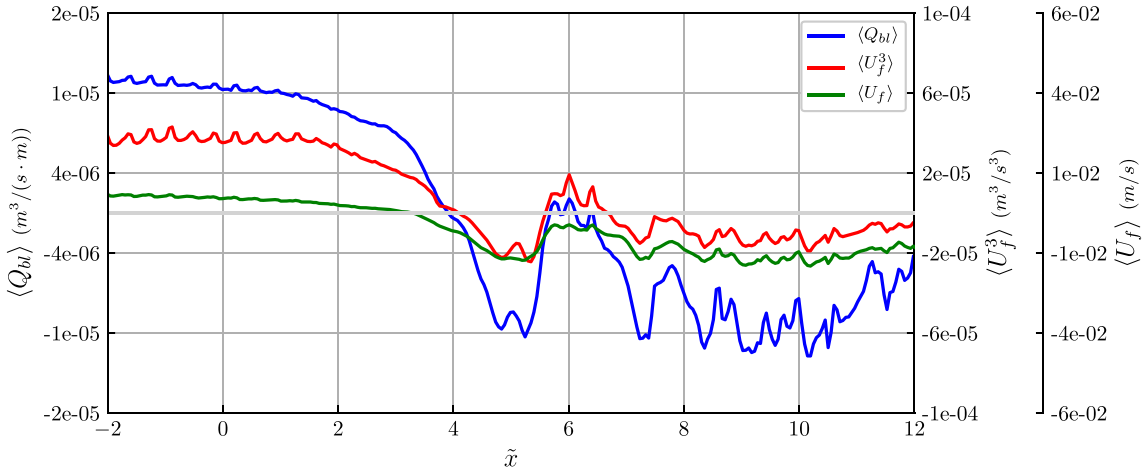

Fig. 6. Distribution of time-averaged bedload transport, friction velocity and cubed friction velocity along the cross-shore profile. Blue line, time-averaged bedload transport. Red line, time-averaged cubed friction velocity. Green line, time-averaged friction velocity. Obtained for waves 100 to 150.

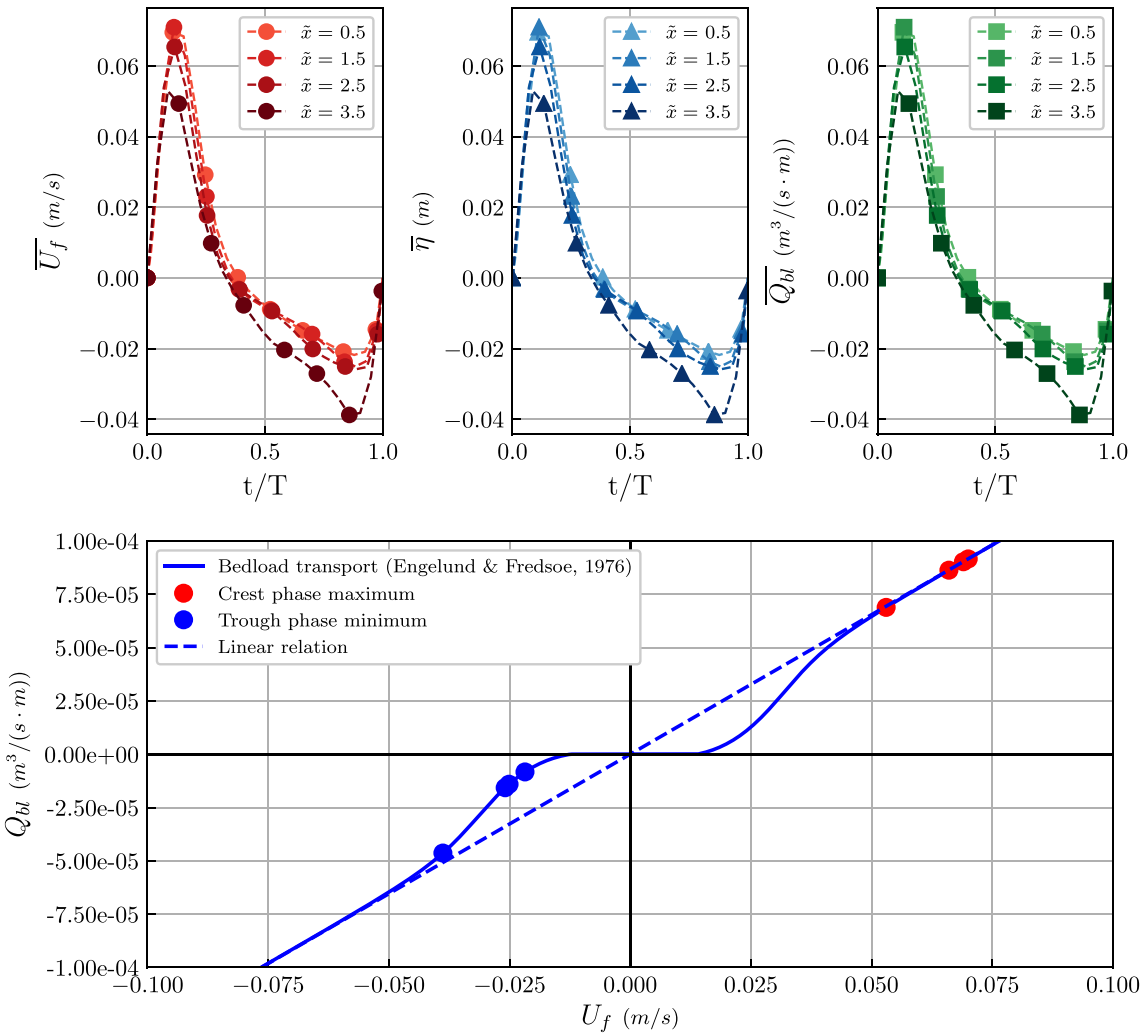

Fig. 7. Top panel (A): phase-averaged free surface, friction velocity and bedload transport obtained at different positions along the outer surf zone. Blue lines, free surface. Red lines, friction velocity. Green lines, bedload transport. Bottom panel (B): relation between friction velocity and bedload transport. The sediment characteristics are the ones of the numerical setup. Blue line, bedload transport (Engelund and Fredsoe, 1976). Blue dashed line, linear relation between bedload transport and friction velocity. Red dots, bedload transport corresponding to the wave crest. Blue dots, corresponding to the wave trough. Obtained for waves 100 to 150.

3.1. Bedload transport

The main hydrodynamic magnitude driving the bedload transport mechanism is the friction velocity (U_f). Formulae such as (Meyer-Peter and Müller, 1948), (Bailard and Inman, 1981) or (Stive, 1986) estimate the bedload transport as a function of the cubed friction velocity. In the numerical model, this relation is maintained by using the empirical formulae from (Engelund and Fredsoe, 1976).

In this section, the relation between bedload transport and friction velocity is further examined to gain more insight into how the accumulation pattern produced by the bedload contribution, shown in Fig. 5A, is produced. Firstly, a time-averaged analysis of the cubed friction velocity and bedload transport distributions along the beach profile is performed. In this way, the influence of hydrodynamic features (currents and wave skewness) in the bedload transport distribution is reflected. Secondly, the remaining factors, related to the interaction between hydrodynamics and sediment transport, are examined in a phase-averaged analysis.

3.1.1. Time-averaged analysis

The time-averaged friction velocity ($\langle U_f \rangle$), cubed friction velocity ($\langle U_f^3 \rangle$) and bedload transport ($\langle Q_{bl} \rangle$) along the beach profile, obtained for waves 100 to 150, are represented in Fig. 6.

For the three variables, maxima, minima and zero-pass occur at roughly the same positions, as can be noted in Fig. 6. The zero-pass of $\langle Q_{bl} \rangle$ in the outer surf zone is an important feature at which the offshore- and onshore-directed transports converge, leading to an accumulation of sediment. The zero-pass of $\langle U_f^3 \rangle$ occurs at the onshore side of that of the friction velocity. This is due to the larger onshore-directed values because of the wave skewness.

Additionally, some important differences in the slope of the three variables can be noted for $2.5 < \tilde{x} < 4.5$ which, according to eq. (7), influence the accumulation of sediment due to bedload transport. The slope of $\langle Q_{bl} \rangle$ increases moderately from $\tilde{x} = 0$ to $\tilde{x} = 2.5$, where it increases sharply until $\tilde{x} = 3.5$, and then decreases again until it changes its sign at $\tilde{x} < 4.5$ approximately. These different slopes in the bedload transport result in a sediment accumulation pattern observed in Fig. 5A, in which the accumulation of sediment increases quickly in $2.5 < \tilde{x} < 3.5$, decreases at a slower rate in $3.5 < \tilde{x} < 4.5$ and then becomes negative (loss of sediment) for $\tilde{x} > 4.5$. Notice that $\langle U_f^3 \rangle$ has a much smoother slope between $\tilde{x} = 0$ and $\tilde{x} = 4.5$. The reasons explaining this pattern are linked to the relation between the friction velocity and bedload transport, as will be explained in the phase-

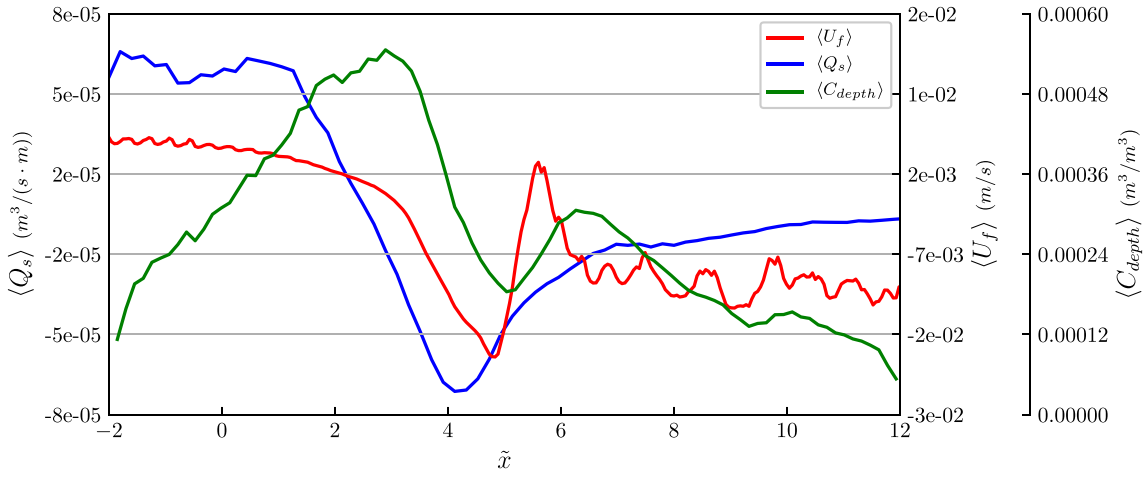

Fig. 8. Distribution of time-averaged suspended transport, friction velocity and depth-averaged sediment concentration along the cross-shore profile. Obtained for waves 100 to 150.

averaged analysis.

3.1.2. *Phase-averaged analysis*

A phase averaged analysis is performed to investigate how the differences between the slopes of $\langle U_f^3 \rangle$ and $\langle Q_{bl} \rangle$ in the interval $0 < \tilde{x} < 4.5$ are related to the varying relation between these magnitudes. The phase-averaged values of friction velocity ($\overline{U_f}$), bedload transport ($\overline{Q_{bl}}$) and free surface ($\overline{\eta}$), obtained for waves 100 to 150 at different positions along the outer surf zone, are shown in Fig. 7.

As can be noted in Fig. 7A, the maximum onshore directed $\overline{U_f}$, corresponding to the wave crest phase, is reduced as waves propagate along the outer surf zone because of the wave breaking process. This can also be noted in $\overline{\eta}$, which also decreases along the outer surf zone. Consistently, $\overline{Q_{bl}}$ is also reduced in the wave crest phase. Regarding the wave trough, the maximum offshore directed $\overline{U_f}$ is nearly the same for $\tilde{x} = 1.5$ and $\tilde{x} = 2.5$, and it increases notably at $\tilde{x} = 3.5$. $\overline{Q_{bl}}$ follows this same trend during the trough phase.

In the wave crest phase, the reduction in $\overline{Q_{bl}}$ and $\overline{U_f}$ as the wave breaking progresses are proportional (linearly related). However, in the wave trough, relatively small increases in $\overline{U_f}$ lead to large variations of $\overline{Q_{bl}}$ (see Fig. 7B). This difference in the relation between friction velocity and bedload transport during the crest and trough phases comes from the separate treatment of the effects of friction velocity in eq. (1): friction velocity influences linearly the velocity at which the moving particles are displaced (U_p) and quadratically the proportion of moving particles (P_{ef}). This aspect is discussed and supported by empirical data in (Engelund and Fredsoe, 1976). For the sediment characteristics of this study case, the relation between friction velocity and bedload transport given by this formula is depicted in Fig. 7B. The relation shown in Fig. 7B can be divided in two regimes: cubic and linear. They are defined based on the relation between friction velocity and bedload transport, which is conditioned by the critical Shields number. For small values of friction velocities that exceed the critical Shields number, the bedload transport scales roughly with the cube of the friction velocity, as it affects both the velocity at which the sediment particles move and the proportion of moving particles. For large values of the friction velocity, the proportion of moving particles reaches a maximum value of 1, and further increases in the friction velocity only affect the velocity at which the particles move, thus being linearly related to the bedload transport.

The maximum friction velocities corresponding to the wave crest phase shown in Fig. 7A are in the linear range, while the velocities of the trough are in the cubic range, as can be noted in Fig. 7B. As the friction velocity during the trough phase does not start to increase until $\tilde{x} = 2.5$, the relation between Q_{bl} and U_f is essentially linear for $\tilde{x} < 2.5$. Consequently, the horizontal gradient of $\langle Q_{bl} \rangle$ is relatively small where $\overline{U_f}$ at the trough phase remains constant ($0 < \tilde{x} < 2.5$). Once $\overline{U_f}$ at the trough phase starts to increase, the associated offshore directed $\overline{Q_{bl}}$ increases cubically, and $\langle Q_{bl} \rangle$ decreases sharply (at $\tilde{x} = 3$ approximately). Note that this sharp variation of the horizontal gradient is not present in $\langle U_f^3 \rangle$.

Therefore, the analysis of the bedload transport shows that the skewness of the friction velocity combined with the different relation between friction velocity and sediment transport during the crest and trough wave phases, which can vary from linear to cubic, leads to a delay in the sharp decay of $\langle Q_{bl} \rangle$ with respect to that of $\langle U_f \rangle$. Firstly, due to the skewness of the friction velocity, the point at which the onshore- and offshore-directed $\langle U_f^3 \rangle$ meet is displaced onshore with respect to that of $\langle U_f \rangle$. Secondly, the decrease in the friction velocity associated to the wave crest, at the onset of wave breaking, has a moderate effect on the bedload transport, as the relation between them is linear. However, increasing the friction velocity of the wave trough that occurs further onshore has a greater effect, as the relation between friction velocity and bedload transport during the trough phase is cubic. For this reason, $\langle Q_{bl} \rangle$ decreases sharply once the friction velocity of the trough phase starts to increase significantly. These two effects lead to an accumulation pattern that produces the growth of the onshore face of the breaker bar on the onshore side of the point where $\langle U_f \rangle$ changes its direction form onshore to offshore.

3.2. *Suspended transport*

The suspended sediment transport depends fundamentally on the relation between velocity and sediment concentration. In a 2D cross-shore profile, these two variables change along the profile and water depth. To examine the overall distribution of suspended transport ($\langle U_f \rangle$), the depth- and time-averaged sediment concentration ($\langle C_{depth} \rangle$) and the depth-integrated and time-averaged suspended transport ($\langle Q_s \rangle$), obtained for waves 100 to 150, are shown in Fig. 8.

$\langle Q_s \rangle$ can be interpreted in a similar way to $\langle Q_{bl} \rangle$: its divergence is the rate of accumulation that it produces. Its negative slope between $\tilde{x} = 0$ and $\tilde{x} = 4$ corresponds to the accumulation zone of suspended transport shown in Fig. 5A obtained from the erosion and deposition rates. Notice that it follows a different trend than $\langle U_f \rangle$ due to the variability of the velocity and sediment concentration along the water depth. Regarding the distribution of $\langle C_{depth} \rangle$ along the cross-shore profile, it can be noted that its maximum ($\tilde{x} = 3$, approximately) does not correspond to those of $\langle U_f \rangle$ or $\langle Q_s \rangle$ and that, overall, it is not directly related to the other two variables due to the variability of sediment concentration distribution

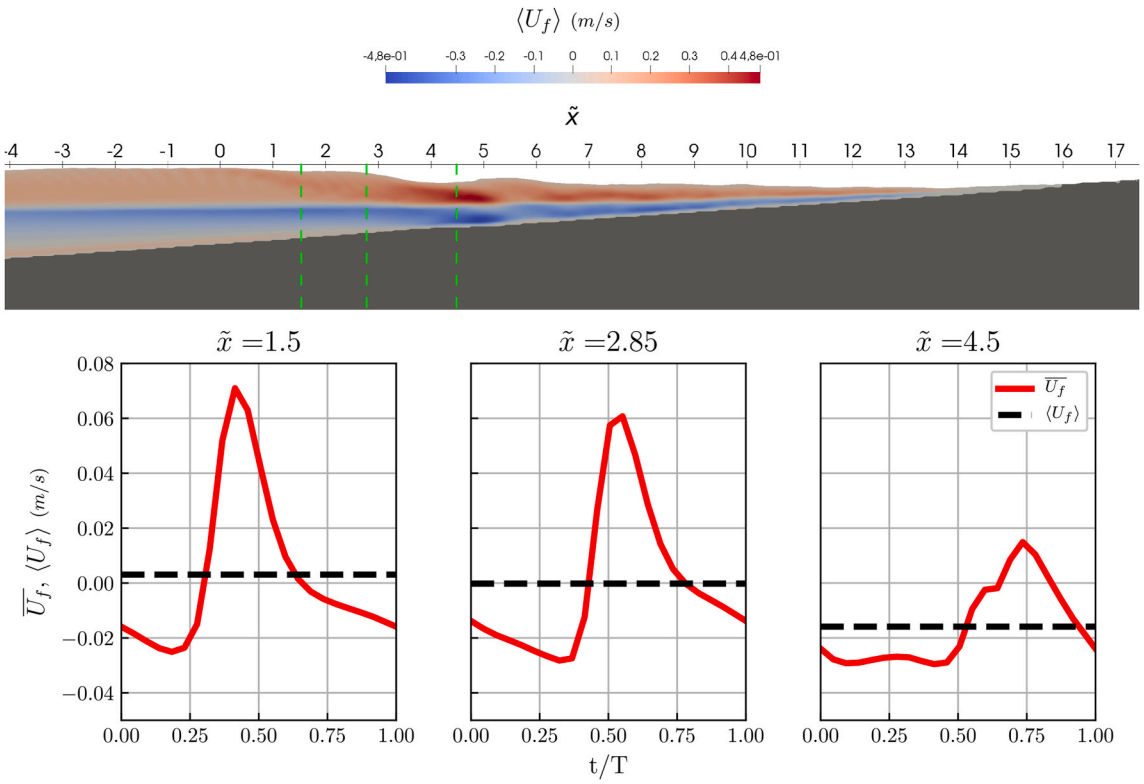

Fig. 9. Phase- and time-averaged friction velocity around the undertow detachment point. Top panel (A), time-averaged velocity field. Bottom panel (B), phase-averaged friction velocity at different locations around the undertow detachment. The velocity fields are obtained for waves 100 to 120, the phase-averaged values for waves 100 to 150.

along the water depth.

A detailed analysis of the processes involved in the suspended transport mechanism requires a 2DV approach to account for the variability of velocity and sediment concentration fields over the water depth. Also, the suspended sediment flux field must be examined. In the following, the main features of these fields are studied in time-averaged terms. However, the time-averaged sediment flux field ($\langle F_{sed} \rangle$) is not directly obtained as the product of the time-averaged velocity and concentration fields ($\langle U \rangle$ and $\langle C \rangle$); intra-wave effects (such as the correlation between velocity and concentration) must be also considered. The importance of these intra-wave effects is highlighted by (Aagard and Jensen, 2013). The analysis of $\langle U \rangle$ and $\langle C \rangle$ captures processes with time scales larger than the wave period, therefore neglecting the intra-wave effects. In contrast, a phase-averaged analysis gives insight into the intra-wave variability. In the following, these two analyses are addressed separately to investigate their effects on the suspended sediment transport.

3.2.1. *Time-averaged analysis of the velocity and concentration fields*

3.2.1.1. Analysis of the velocity field. Time-averaging the velocity field allows to analyse the currents present in the cross-shore profile. Fig. 9A shows the time-averaged velocity field ($\langle U \rangle$). Similar time-averaged velocity fields were obtained from laboratory experiments (e.g.

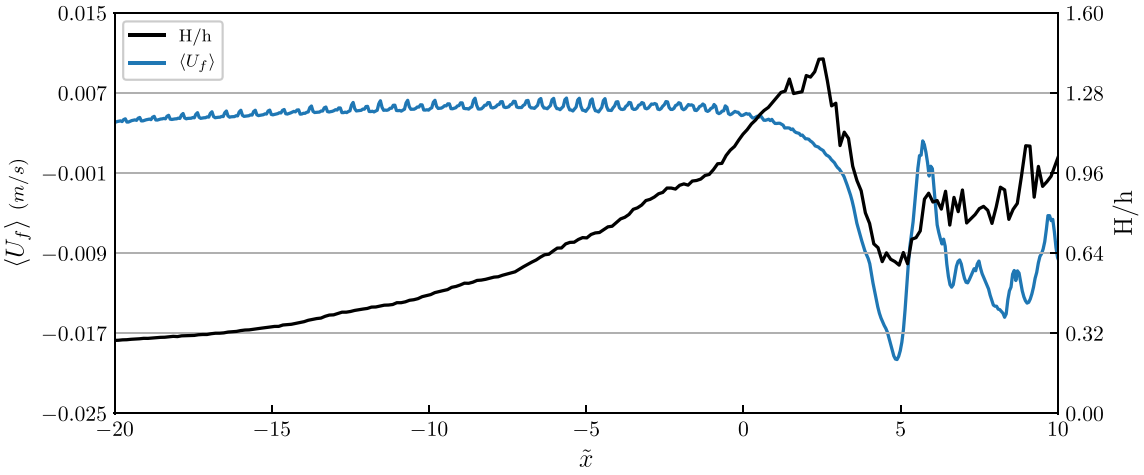

Fig. 10. Distribution of time-averaged friction velocity along the cross-shore profile, reflecting the effect of the steady streaming. Blue line, time-averaged friction velocity obtained for waves 100 to 150. Black line, relative wave height obtained for waves 100 to 150.

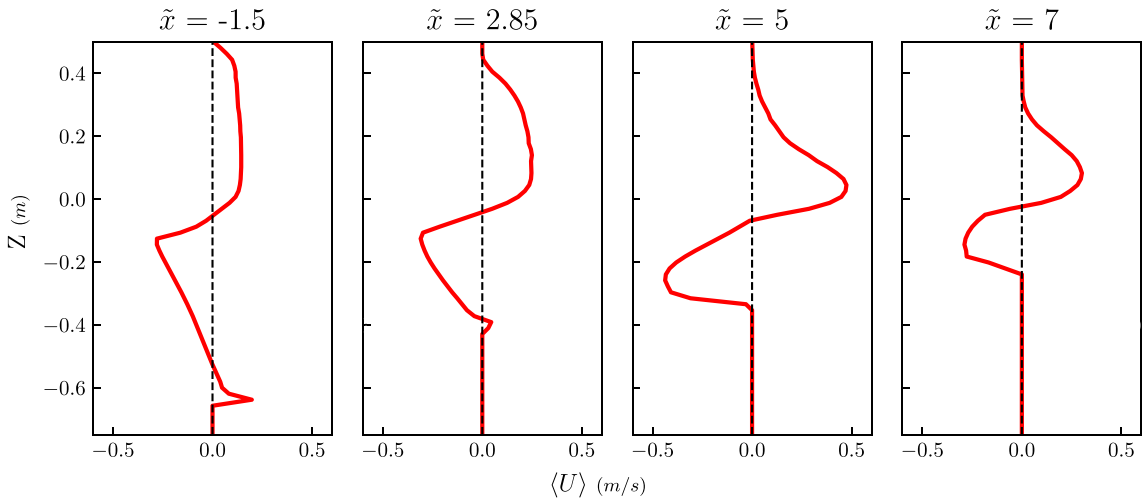

Fig. 11. Time-averaged velocity profiles along the cross-shore profiles obtained for waves 100 to 150.

(Okayasu et al., 1986), and (Tajima and Madsen, 2006)).

Two types of near-bed currents are identified in Fig. 9A: a steady streaming in the shoaling and outer surf zones (onshore-directed, red coloured) and an undertow in the inner surf zone (offshore-directed, blue coloured).

The steady streaming is produced by two competing effects according to (Holmedal & Myrhaug, 2009). On the one hand, the progressive wave steady streaming, due to the non-zero vertical near-bed velocities, enhances onshore transport and increases when the water depth is reduced. On the other hand, the wave skewness effect on turbulent viscosity, produced by the difference in turbulent viscosity between crest and trough wave phases, enhances the offshore sediment transport and increases with wave skewness. The relative wave amplitude (a/h) also influences the magnitude of the steady streaming, with higher steady streaming being produced by a larger relative wave amplitude (Kranenburg et al., 2013). Then, the steady streaming is expected to be maximum along the shoaling zone, close to the break point, due to the increase in relative wave amplitude and reduced water depth, although the high wave skewness of the waves close to breaking can partially compensate these effects.

The analysis of the distribution of the steady streaming along the shoaling and outer surf zones can be performed by looking at $\langle U_f \rangle$, which is representative of the strength of the near-bed current. As waves are highly non-linear when they approach the breaking point, the relative wave height (H/h) is used in this analysis instead of the relative wave amplitude used in previous studies. Fig. 10 shows $\langle U_f \rangle$ and H/h along the cross-shore profile, both obtained for waves 100 to 150.

The increasing $\langle U_f \rangle$ along the shoaling zone ($\tilde{x} < 0$), reflects the enhancement of the steady streaming due to the increase in H/h. The maximum onshore-directed current occurs at $\tilde{x} = -3$ approximately. Further onshore, the undertow and increasing wave skewness partially compensate the steady streaming, and $\langle U_f \rangle$ remains nearly constant. Once the waves start to break (at $\tilde{x} = 0$), the steady streaming decreases rapidly, although H/h keeps increasing along the outer surf zone until $\tilde{x} = 3$, approximately (see Fig. 2). This is due to the further reduction in water depth, which decreases faster than the wave height right after the wave breaking process starts, so that H/h increases despite the wave height being smaller. The increase of $\langle U_f \rangle$ along the shoaling zone explains why the accumulation zone of suspended transport starts at $\tilde{x} = 0$ (as shown in Fig. 5A): the increasingly strong steady streaming does not let the sediment eroded by the shoaling waves settle, but rather advects it towards the surf zone. Once the steady streaming starts decreasing, part of the sediment advected by it settles, contributing to the growth of the breaker bar.

Regarding the second type of near-bed current identified in Fig. 9A, the undertow, it compensates the onshore-directed mass flow rate induced by the crests of breaking waves and steady streaming, so that the mean water flux across each section of the cross-shore profile is zero (if the mean water level already reaches its equilibrium configuration). Therefore, its mass flux is determined by that induced by the breaking waves crests and the steady streaming. Also, for a given mass flux and due to mass conservation, the mean (time- and depth averaged) velocity of the undertow depends on the cross-sectional area it flows across. Additionally, for the same mean velocity, the velocity profile might change its shape depending on the distribution of the stresses along the water depth, resulting in larger or smaller velocities close to the seabed (Svendsen, 1984).

At a certain point in the outer surf zone, these two near-bed currents (undertow and steady streaming) meet and compensate each other in time-averaged terms. This point is named undertow detachment, and it was experimentally observed by (Longuet-Higgins, 1983). As discussed by (Longuet-Higgins, 1983), the undertow detachment is an important feature for the suspended sediment transport as the convergence of the two main near-bed currents, carrying suspended sediment, may result in an accumulation of sediment at that point. It also corresponds to the zero pass of $\langle U_f \rangle$, as the friction velocity and the near-bed velocity are linearly related according to the velocity profile of a boundary layer. In this case, the undertow detachment can be identified in the distribution of $\langle U_f \rangle$, presented in Fig. 8, at $\tilde{x} = 2.85$. An important caveat regarding the undertow detachment is that the value of the instantaneous near-bed velocities at it can be quite high despite the time-averaged value being zero. To illustrate this feature, the phase-averaged friction velocities ($\overline{U_f}$) at the undertow detachment point and on the onshore and offshore sides of it are analysed and represented in Fig. 9B along with the corresponding $\langle U_f \rangle$.

Fig. 9B shows high values of $\overline{U_f}$ at and near the undertow detachment point. At $\tilde{x} = 1.5$ during the wave trough phase, $\overline{U_f}$ is high and offshore-directed despite $\langle U_f \rangle$ being onshore-directed (the undertow is already detached from the seabed). At the undertow detachment point ($\tilde{x} = 2.85$), $\overline{U_f}$ in the wave crest and in the wave trough phases is quite large, even though $\langle U_f \rangle$ is zero. On the onshore side of the undertow detachment ($\tilde{x} = 4.5$) $\langle U_f \rangle$ is offshore-directed, while the maximum $\overline{U_f}$ is positive (onshore-directed) corresponding to the wave crest phase. These high friction velocities generated during the crest and trough phases are quite relevant, as they put a significant amount of sediment in suspension.

To further analyse the currents in the cross-shore profile, $\langle U \rangle$ profiles at different positions are shown in Fig. 11.

The undertow and steady streaming can be clearly observed in

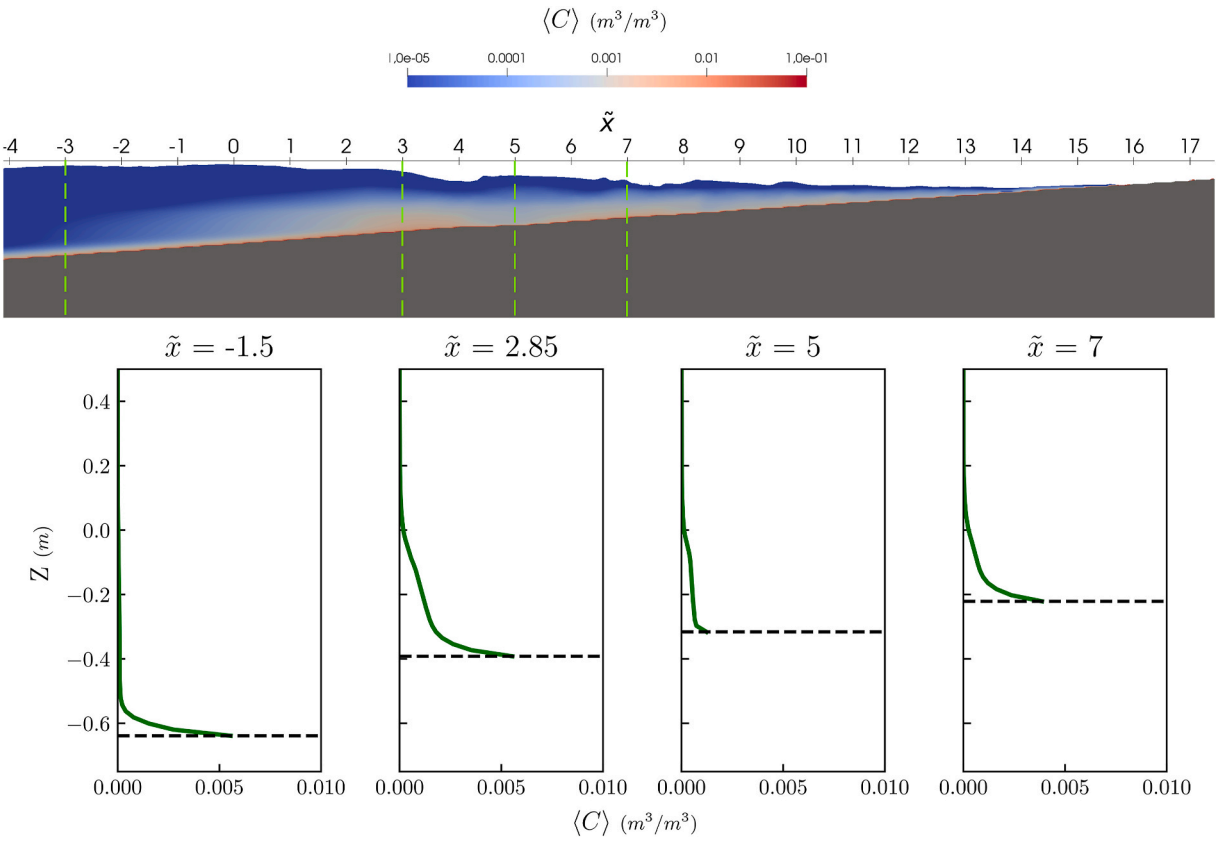

Fig. 12. Top panel (A), time-averaged concentration field. Bottom panel (B), time-averaged concentration profiles at different positions along the cross-shore profile. The concentration field is obtained for waves 100 to 120, the time-averaged profiles for waves 100 to 150.

Fig. 11. On the offshore side of the undertow detachment point, the influence of the steady streaming is stronger than the undertow near bed. This leads to onshore directed $\langle U \rangle$ close to the seabed. However, the undertow is still present far from it (detached undertow). In contrast, on the onshore side of the undertow detachment, the undertow produces offshore directed $\langle U \rangle$ close to the seabed. The balance between the onshore-directed water mass flux produced by the wave crests and steady streaming, and the offshore-directed due to the undertow can be also noted. According to this idea of compensation between onshore- and offshore-directed fluxes, the maximum mean undertow velocity occurs on the onshore side of the plunge point (at $\tilde{x} = 5.8$ in this case), as the mass flux produced by the breaking waves is also maximum at this position. In Fig. 11, it can be noted that the undertow velocity is higher close to the plunge point at $\tilde{x} = 5$, also in the $\langle U \rangle$ fields of Fig. 9A.

The aforementioned influencing factors on the undertow and steady streaming (mass flux produced by the wave crests, water depth, distribution of Reynold's stresses, wave height and wave skewness) can enhance or weaken them, effectively displacing the position of the undertow detachment and the zone where the sediment is accumulated. For instance, a variation of the undertow velocity profile resulting in larger near-bed velocities caused by a redistribution of the Reynold's stresses along the water depth would displace the undertow detachment seawards, and the sediment would start to accumulate at this new position. Therefore, variation of these factors, such as the ones produced by changes in the bathymetry, wave conditions, mean water level and others, modify the way in which the evolution of the beach profile occurs.

Additionally, the reasons for the location of the breaker bar inside the outer surf zone can be derived from the analysis of these influencing factors. In a plane bathymetry with a certain slope, the undertow has a maximum velocity close to the plunge point and decreases as moving offshore due to the increase in water depth (as can be observed in Fig. 9A and Fig. 11). Additionally, the steady streaming has its maximum velocity at the break point and decreases quickly in the outer surf zone (see Fig. 10). From these observations, it can be concluded that the position at which the undertow is compensated by the steady streaming (the undertow detachment point) is located between the break and plunge points (as shown in Fig. 9). Consistently, the main accumulation of sediment leading to the growth of the breaker bar is produced at that position (Fig. 5A).

3.2.1.2. Analysis of the sediment concentration field. To examine the distribution of the sediment concentration in the cross-shore profile, the time-averaged sediment concentration field ($\langle C \rangle$) is obtained and depicted in Fig. 12A. $\langle C \rangle$ profiles at different locations along the cross-shore profile are also given in Fig. 12B.

In the shoaling zone, the sediment concentration is present only close to the seabed, as can be noted in Fig. 12B at $\tilde{x} = -3$. In contrast, in the inner surf zone, the vortices generated during the wave breaking process produce a strong mixing of sediment and keep it in suspension ($\tilde{x} = 5$ and $\tilde{x} = 7$), as suggested by (Ting and Kirby, 1995). Despite the limitations of RANS models to provide detailed results of the turbulent fluctuations, the mixing effect of the vortices resulting from wave breaking in the inner surf zone is captured by the numerical model (see (García-Maribona et al., 2021). Regardless of the strong mixing in the inner surf zone, the $\langle C \rangle$ profile is still far from uniform, being $\langle C \rangle$ much higher close to the seabed than in the upper layers. In the outer surf zone ($0 < \tilde{x} < 5$), there is also a high mixing of sediment, although the breaking-induced eddies do not affect this zone. This feature was reported in previous studies such as the experimental study performed by (Wang et al., 2002), and it can be related to the strong vertical velocities generated during the breaking process. This explains the influence of the type of wave breaking mechanism (spilling or plunging) in the sediment concentration distribution, observed by (Wang et al., 2002) for the outer

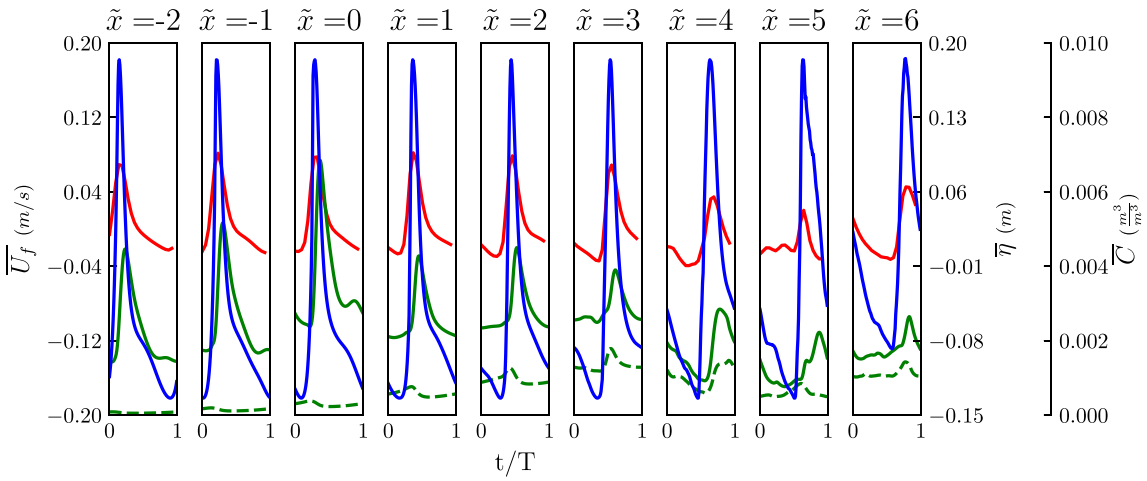

Fig. 13. Phase-averaged concentration, free-surface and friction velocity. Green line, near-bed concentration (continuous line) and half-depth concentration (dashed line). Blue line, free surface. Red line, friction velocity. Obtained for waves 100 to 150, the near-bed concentrations are obtained at 5 cm from the seabed.

surf zone. The large amount of sediment put in suspension in the outer surf zone, close to the seabed, together with the mixing effect of the vertical velocities of the wave breaking process, results in a high $\langle C \rangle$ along the water column in the outer surf zone, as can be noted in Fig. 12B at $\tilde{x} = 3$.

Therefore, the distribution of $\langle C \rangle$ is a consequence of the different mixing mechanisms acting in each part of the cross-shore profile. In the shoaling zone, the weak diffusive mixing due to near-bed turbulence, which decreases as moving far from the seabed, is not enough to overcome the sediment fall velocity, and the sediment stays in a thin layer close to the seabed. In the outer surf zone, the vertical velocities produced by the breaking process lift sediment from the lower layers to the upper ones. Finally, in the inner surf zone, a strong mixing is produced by the wave breaking induced vortices leading to a more uniform distribution in the water column. These differences in $\langle C \rangle$ distribution on the water column for breaking and non-breaking waves (corresponding to the shoaling and inner surf zones, respectively) are in agreement with previous laboratory studies (e.g. (Nielsen et al., 1978),) and with field data (e.g. (Ogston and Sternberg, 2002),). The distribution of $\langle C \rangle$ along the water column has important implications in the suspended sediment transport, as will be discussed in the analysis of time-averaged sediment fluxes. Depending on the shape of the $\langle C \rangle$ profiles, more or less sediment

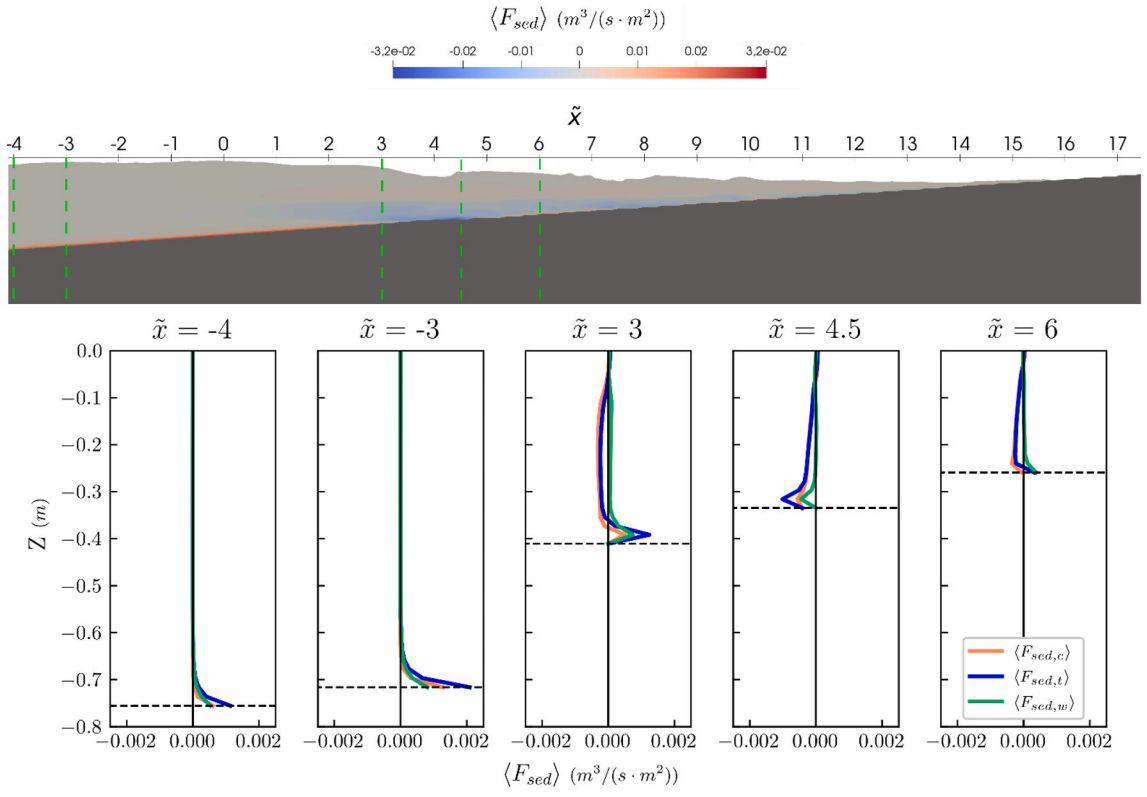

Fig. 14. Top panel (A): Time-averaged horizontal sediment flux field. Bottom panel (B): time-averaged horizontal sediment flux profiles at different positions. Blue line, total sediment flux. Orange line, sediment flux due to currents. Green line, sediment flux due to waves. The sediment flux field is obtained for waves 100 to 120, the time-averaged profiles for waves 100 to 150.

concentration is subjected to the effect of the currents described in analysis of $\langle U \rangle$.

3.2.2. Intra-wave analysis of velocity and concentration fields

The key aspect regarding in intra-wave variability is the correlation between velocity and concentration. Highly correlated velocity and concentration results in a large suspended transport, as the peak values of velocity and concentration occur at the same time. To analyse this aspect, the phase-averaged free-surface ($\overline{\eta}$), friction velocity ($\overline{U_f}$) and sediment concentration ($\overline{C}$) for different points close to the seabed (5 cm from it) and at half depth, obtained for waves 100 to 150, are shown in Fig. 13. Similar results were obtained in previous studies carried out in the field (e.g. (Aagard and Jensen, 2013),).

Fig. 13 shows that $\overline{\eta}$ and $\overline{U_f}$ are highly correlated along the shoaling and outer surf zones ($\widetilde{x} < 0$ and $0 < \widetilde{x} < 5$, respectively) and their high correlation still holds at the plunge point ($\widetilde{x} = 5$) for the crest-phase. In the outer surf zone, $\overline{C}$ close to the seabed (continuous green line) is correlated with $\overline{\eta}$ and $\overline{U_f}$, while it is uncorrelated or even negatively correlated for half-depth (dashed green line). At half-depth, for $\widetilde{x} < 3$, $\overline{C}$ is negatively correlated to the $\overline{\eta}$ and $\overline{U_f}$ (high concentrations occur at the wave trough instead of wave crest phase). This implies that $\langle F_{sed} \rangle$ is offshore directed in the upper layers of the outer surf zone while it is onshore directed in the lower ones. As will be shown in the next section, this has important implications on the circulation of suspended sediment in the outer surf zone.

Considering the previously described $\langle U \rangle$ and $\langle C \rangle$ fields, some important aspects concerning the numerical modelling of sediment transport for beach morphodynamics can be extracted. In the shoaling zone, the suspended sediment concentration far from the seabed is very low due to the absence of strong mixing processes. Thus, assuming the suspended transport to be fully contained in a thin layer close to the seabed in which it has a constant value (behaving like a one-dimensional feature) is not too far from reality. Additionally, the velocity and concentration are highly correlated close to the seabed and neglecting the intra-wave effects does not introduce great errors in the results. For these two reasons, the suspended transport in the shoaling zone behaves similarly to the bedload transport, and some of the 1D numerical models using averaged transport rates can predict the evolution of the shoaling zone with suitable accuracy by introducing calibration factors, even if they do not have a separated treatment of the bedload and suspended contributions. However, in the surf zone these two simplifications (assume 1D and neglecting intra-wave effects) are no longer valid, which explains the limited skill that these models present in the predictions of surf zone morphodynamics (e.g. (Kalligeris et al., 2020), (Ruffini et al., 2020)).

3.2.3. Time-averaged suspended sediment flux

To investigate how the suspended sediment circulates in the cross-shore profile as a result of the velocity and concentration distributions and intra-wave effects, the $\langle F_{sed} \rangle$ field is obtained by first calculating its instantaneous value (as the product of instantaneous velocity and concentration fields) and then, performing the time-averaging of the result. The horizontal component of the total $\langle F_{sed} \rangle$ ($\langle F_{sed,t} \rangle$) and those produced by currents ($\langle F_{sed,c} \rangle$) and by intra-wave effects ($\langle F_{sed,w} \rangle$) are presented in Fig. 14.

In the shoaling zone ($\widetilde{x} < 0$), close to the break point, there is a strong, near-bed, onshore-directed $\langle F_{sed,t} \rangle$ ($0.002 \frac{m^3}{m^2 \cdot s}$ approximately at $\widetilde{x} = -3$). This is consistent with the combination of steady streaming and high near-bed concentrations (shown in Figs. 9 and 12, respectively), and with highly correlated concentration and velocity fields (shown in Fig. 13). As moving offshore, $\langle F_{sed,t} \rangle$ decreases due to the smaller wave height and near-bed concentrations (see $\widetilde{x} = -4$ in Fig. 14B curves $\langle F_{sed,c} \rangle$ and $\langle F_{sed,w} \rangle$, respectively).

For the outer surf zone ($0 < \widetilde{x} < 5$), the near-bed current advecting the sediment depends on whether the undertow is attached (therefore it is advected offshore) or detached (advected onshore by the steady streaming). These two near-bed suspended transports meet at the undertow detachment producing an accumulation of sediment in accordance with what was suggested by (Longuet-Higgins, 1983). However, the high correlation between velocity and concentration close to the seabed favours the onshore transport produced by the steady streaming, pushing this point to the onshore side of the undertow detachment (at $\widetilde{x} = 3$ there is still onshore-directed transport close to the seabed). Additionally, along the outer surf zone, the sediment concentration far from the seabed is advected offshore by the detached undertow, towards the shoaling zone. The existence of a significant offshore-directed sediment flux far from the seabed at the break point was also observed in the laboratory, especially under plunging breakers (e.g. (Wang et al., 2003), and (Wang et al., 2002)). This sediment flux increases with larger sediment concentration in the upper layers of the outer surf zone (more uniform concentration profiles) and with higher velocity of the detached undertow. This sediment flux increases the extent of the suspended transport accumulation zone to the offshore side of the undertow detachment point, therefore contributing to the growth of the offshore face of the breaker bar.

In the inner surf zone, there is an onshore-directed sediment flux close to the seabed for $5 < \widetilde{x} < 7.5$ approximately, which can be also observed in the $\langle F_{sed,t} \rangle$ profile at $\widetilde{x} = 6$. However, $\langle U \rangle$ is only positive in a small portion of this area, as can be noted in the distribution of $\langle U_f \rangle$ depicted in Fig. 10. Intra-wave effects (represented by $\langle F_{sed,w} \rangle$) are responsible for this difference, as can be noted in Fig. 14B: the sediment concentration and velocity close to the seabed are highly correlated during the wave crest phase but not during the wave trough phase in this zone (as shown in Fig. 13). Thus, the onshore-directed velocities carry more sediment than the offshore-directed ones resulting in a net onshore-directed transport on a larger area than that affected by onshore-directed $\langle U \rangle$. For the rest of the inner surf zone ($\widetilde{x} > 7.5$), there is a high near-bed, offshore-directed transport due to the presence of the undertow and a low onshore-directed transport in the upper layers produced by the crests of broken waves. The offshore-directed $\langle F_{sed,t} \rangle$ is relatively small ($-0.001 \frac{m^3}{m^2 \cdot s}$, approximately) compared to the onshore-directed observed in the shoaling zone close to the break point, as C is smaller and less correlated to the velocity during the wave trough phase (see Fig. 13).

Finally, the intra-wave effects, represented by $\langle F_{sed,w} \rangle$, are more significant close to the seabed where the correlation between sediment concentration and velocity is higher. Note that in the shoaling zone ($\widetilde{x} < 0$), $\langle F_{sed,w} \rangle$ is almost as high as $\langle F_{sed,c} \rangle$. Consistently with the previous discussion, at $\widetilde{x} = 6$ the intra-wave effects change the direction of $\langle F_{sed,t} \rangle$ from offshore-to onshore-directed. In contrast, $\langle F_{sed,w} \rangle$ is almost negligible far from the seabed, where the sediment flux is rather driven by currents.

Considering the $\langle F_{sed,t} \rangle$ field, shown in Fig. 14A, the circulation of sediment in the outer surf zone can be summarized as follows. The high friction velocity produced by breaking waves puts sediment in suspension, which is lifted by the strong vertical velocity occurring during the wave breaking process to the upper layers of the outer surf zone. Then, the detached undertow advects this sediment towards the shoaling zone. Once this sediment settles by gravity, it can be either captured by the steady streaming (for sediment falling on the offshore side of the breaking point) and advected back to the outer surf zone, or it can directly settle in the outer surf zone. In both cases, the sediment transport produced by the detached undertow contributes to the accumulation of sediment along the offshore face of the breaker bar, as observed in Fig. 5A.

3.3. Influence of the breaker type

The wave conditions (height and period) clearly influence the

Table 2
Test conditions for analysing the influence of the Iribarren number.

Test case	Wave height (m)	Wave period (s)	Ir_0 (−)	Plunge ($\tilde{x}$)	Undertow detachment ($\tilde{x}$)	Break ($\tilde{x}$)
1	0.43	2.7	0.34	6.81	4.96	1.01
2	0.43	3.7	0.47	5.85	2.87	0.00
3	0.43	4.7	0.60	5.19	2.18	−1.16

aforementioned hydrodynamic processes driving the sediment transport mechanisms. To analyse their influence in the sediment transport rates, a comparison between three different wave conditions is presented. The three test cases are set maintaining the same wave height and changing the wave period to achieve different Iribarren numbers, aiming to provide a representation of plunging and spilling breakers. The results for the three test cases are also obtained for waves 100 to 150, so that the three wave conditions can be compared despite the different wave periods. Additionally, the normalized position along the cross-shore profile is obtained using the position and water depth of the break point corresponding to the case with wave period equal to 3.7 s. The test conditions and the position of relevant points are given in Table 2.

The distribution of the wave height along the cross-shore profile for the three tests is shown in Fig. 15.

The results in Fig. 15 show that higher Iribarren numbers result in a larger wave height at the break point, which is displaced offshore. In addition, for plunger breakers the wave height starts decreasing smoothly, but then it drops sharply (green line in Fig. 15). At the plunge point, high Iribarren numbers produce a second peak in the wave height distribution (at $\tilde{x} = 5$, approximately), whereas it does not appear in spilling breakers.

3.3.1. *Bathymetric evolution*

The first step for the comparison of the three Iribarren numbers is to examine the differences in the resulting bathymetry. For this purpose, the bathymetric evolution of the three test cases is represented in Fig. 16.

As can be noted, there are some similarities in the bathymetric evolution of the three cases. Consistently with the previous discussion on the sediment accumulation patterns, in all of them the breaker bar is generated around the undertow detachment point, being limited by the break point on the offshore side and by the plunge point on the onshore side. As the Iribarren number increases, the break, plunge and undertow detachment points are displaced seawards, and the breaker bar is generated further offshore. Additionally, a larger Iribarren number leads to a quicker development of the breaker bar and trough.

The evolution of the position of the breaker bar front presents important differences among the three test cases. In Fig. 17, the evolution of the position of the breaker bar front along each simulation, obtained as the intersection between the bathymetry and the initial profile, is displayed.

Fig. 17 shows different migration speeds of the breaker bar. For low

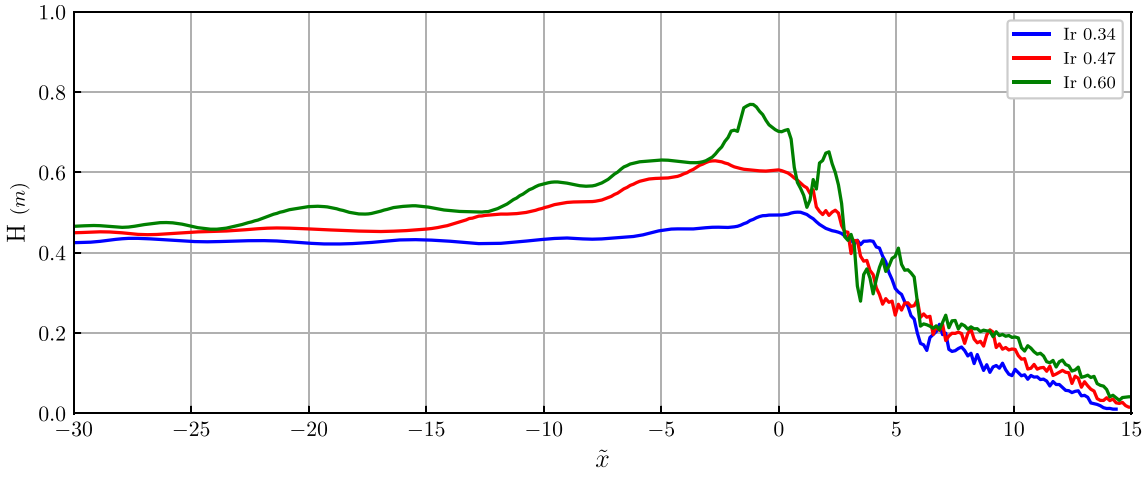

Fig. 15. Distribution of wave height along the beach profile for the three test cases. Obtained for waves 100 to 150.

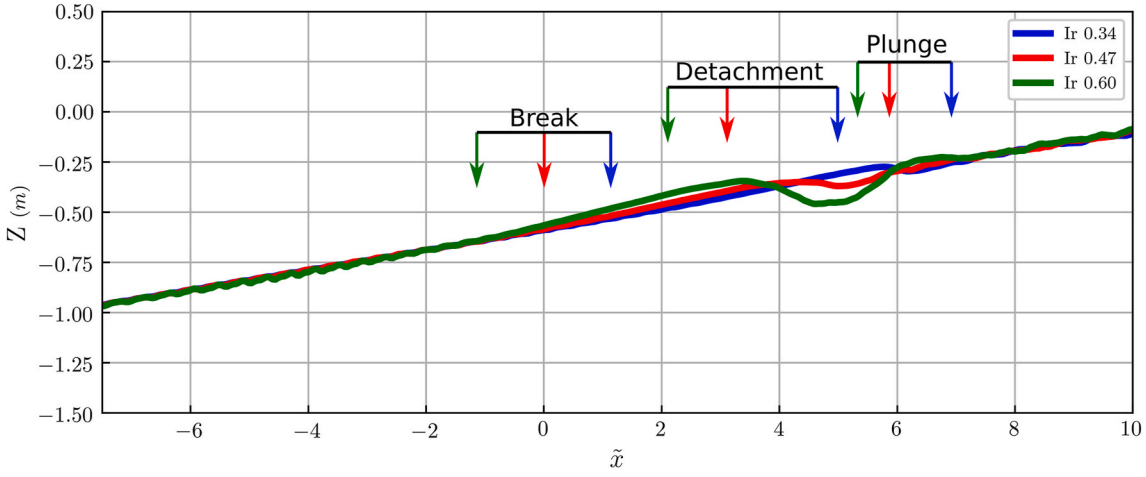

Fig. 16. Bathymetry after 150 waves for the three test cases. The arrows show the location of the break, undertow detachment and plunge points for the three cases.

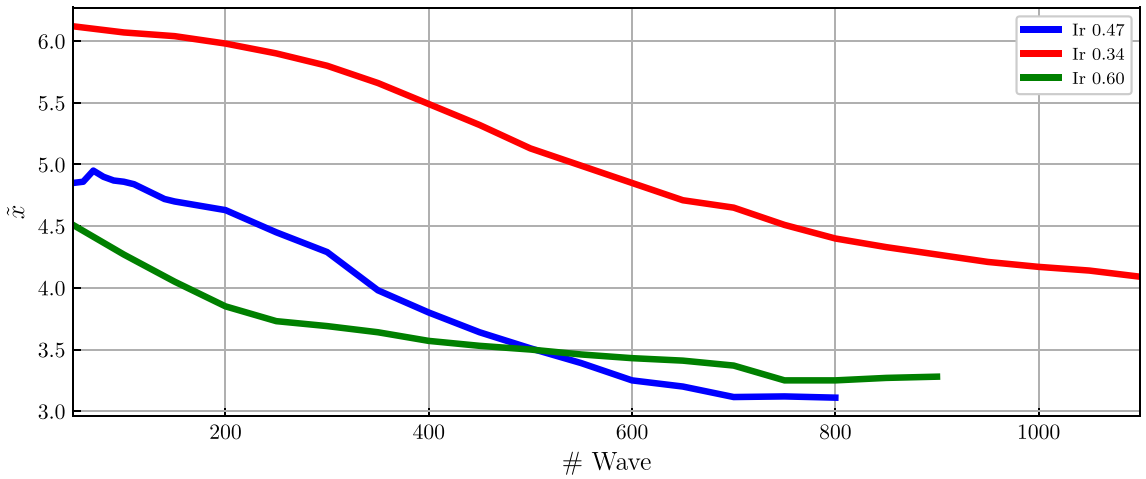

Fig. 17. Evolution of the position of the onshore face of the breaker bar for the three test cases. Obtained until the equilibrium status is achieved.

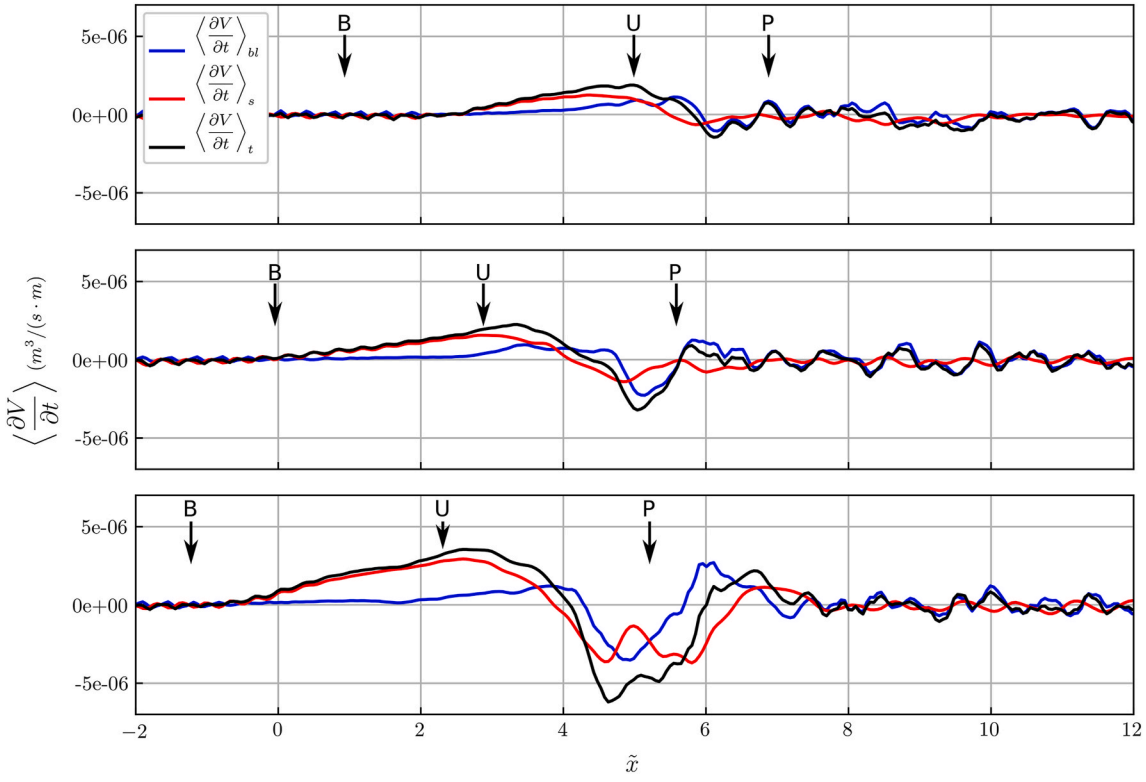

Fig. 18. Accumulation rates for the three wave conditions obtained from waves 100 to 150. Top panel, Iribarren 0.34. Centre panel, Iribarren 0.47. Bottom panel, Iribarren 0.60. The break (B), undertow detachment (U) and plunge (P) points are also represented with arrows.

Iribarren numbers, the breaker bar migrates slower and has an initial stage in which the breaker bar grows but stays at roughly the same position. In contrast, the plunging breakers quickly lead to the migration of the breaker bar, without a previous growth stage. Additionally, the equilibrium profile is reached after less waves for higher Iribarren numbers. Overall, the evolution of the cross-shore profile occurs faster for plunging than for spilling breakers, which is to be expected, and the duration of the growth stage is smaller (non-existing for the test case with Iribarren 0.60).

In the following analysis, the differences between these three test cases are addressed using the previously discussed processes. Firstly, the time-averaged sediment transport rates corresponding to them are represented in Fig. 18.

As can be observed in Fig. 18, both the suspended and bedload transport contributions accumulate sediment in the outer surf zone in all the cases, which leads to the generation of the breaker bar. As the Iribarren number increases, the total sediment transport increases as well, and the accumulation zone moves offshore. The bedload transport accumulates sediment mainly on the onshore side of the undertow detachment while the suspended contribution accumulates sediment on the offshore side, which is in accordance with the previous discussion. Additionally, the suspended transport produces erosion at the plunge point for the intermediate and plunging breakers, while this does not happen under spilling breakers.

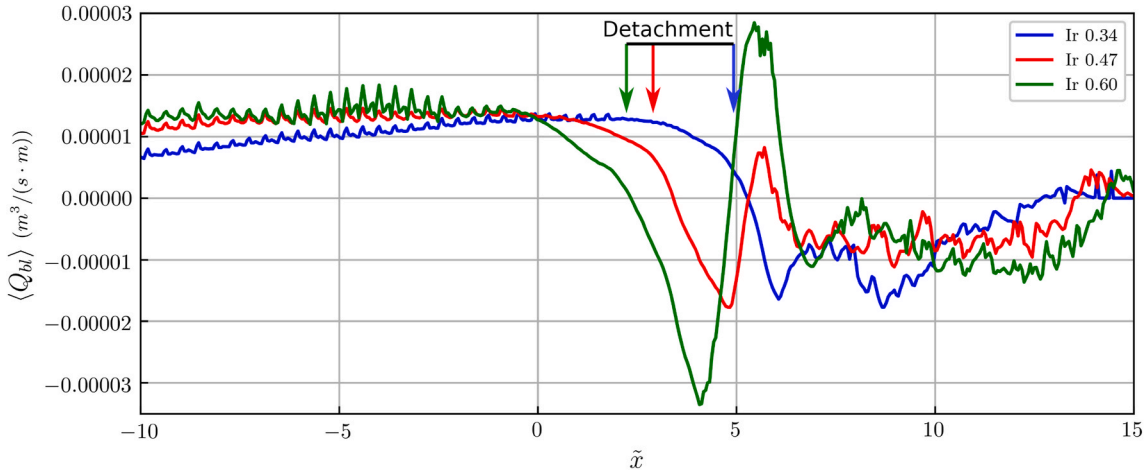

Fig. 19. Distribution of time-averaged bedload transport along the cross-shore profile for the three test cases. Obtained for waves 100 to 150.

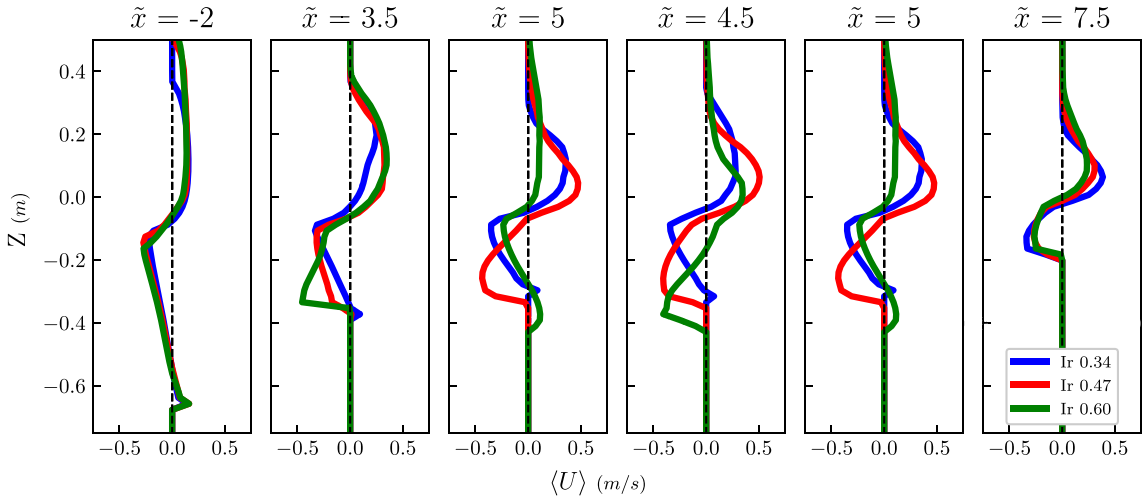

Fig. 20. Time-averaged velocity profiles at different positions along the beach profile. Obtained for waves 100 to 150.

3.3.2. *Bedload transport*

Fig. 18 shows that the magnitude of the accumulation produced by the bedload transport is similar in all three test cases, and it occurs farther offshore as the Iribarren number increases. To further investigate this aspect, the distribution of $\langle Q_{bl} \rangle$ is shown in Fig. 19.

Fig. 19 shows that the variation in the horizontal gradient of $\langle Q_{bl} \rangle$ which leads to the main accumulation of sediment is present in the three cases. It starts approximately at the position of the undertow detachment, producing the main accumulation of sediment at its onshore side. It can be also observed that the offshore-directed transport in the outer surf zone is higher for plunging breakers due to an increase in $\langle U \rangle$ close to the seabed. These higher velocities are responsible for the faster growth of the bar trough at higher Iribarren numbers. Another aspect enhanced in plunging breakers is the onshore-directed transport produced landwards the plunge point ($\tilde{x} = 6$ approximately), which is to be expected as the plunging jet produces high velocities when it reaches the seabed. Notice that this does not occur for spilling breakers (blue line in Fig. 19). For the inner surf zone, $\langle Q_{bl} \rangle$ is lower at high Iribarren numbers, as the undertow is reduced due to the higher momentum mixing produced by the eddies (Ting and Kirby, 1995), (Ting and Nelson, 2011). In the swash zone, $\langle Q_{bl} \rangle$ induced by the spilling breakers becomes the smallest of the three cases. This is consistent with the higher energy dissipation that results in smaller wave height in this zone (as shown in Fig. 15), leading to a weaker undertow.

These observations in $\langle Q_{bl} \rangle$ can be explained from the variations of the $\langle U \rangle$ profiles close to the seabed; these are shown in Fig. 20.

The increase of $\langle U \rangle$ with the Iribarren number in the outer surf zone can be clearly observed at $\tilde{x} = 3.5$ and $\tilde{x} = 4$. The velocity profile is shifted downwards under the plunging breakers (green line), so that $\langle U \rangle$ decreases in the upper layers of the outer surf zone and increases closer to the seabed. This change in the shape of the undertow profile can be related to the breaker type and to the bathymetry shape. Under plunging breakers, the undertow is forced to flow in the lower layers of the flow, as the upper ones are highly mixed and subjected to high onshore-directed velocities during the wave-crest phase due to the plunging jet (which loses energy as it penetrates in the lower layers). In contrast, for spilling breakers, the momentum mixing along the water depth is much smaller, and the onshore-directed velocities of the wave crests occur only close to the mean water level. Additionally, as the bar trough is already developed and has a significant depth, the lower layers of the outer surf zone (closer to the seabed) are less influenced by the impinging jet, thus the water flux exiting the surf zone flows at higher velocities close to the seabed. Finally, the reduction in undertow velocity in the inner surf zone for the high Iribarren numbers can be observed at $\tilde{x} = 7.5$, the undertow produced by the spilling breakers is stronger than those of the intermediate and plunging cases due to the lower momentum mixing along the water column, as explained in (Ting and Kirby, 1994).

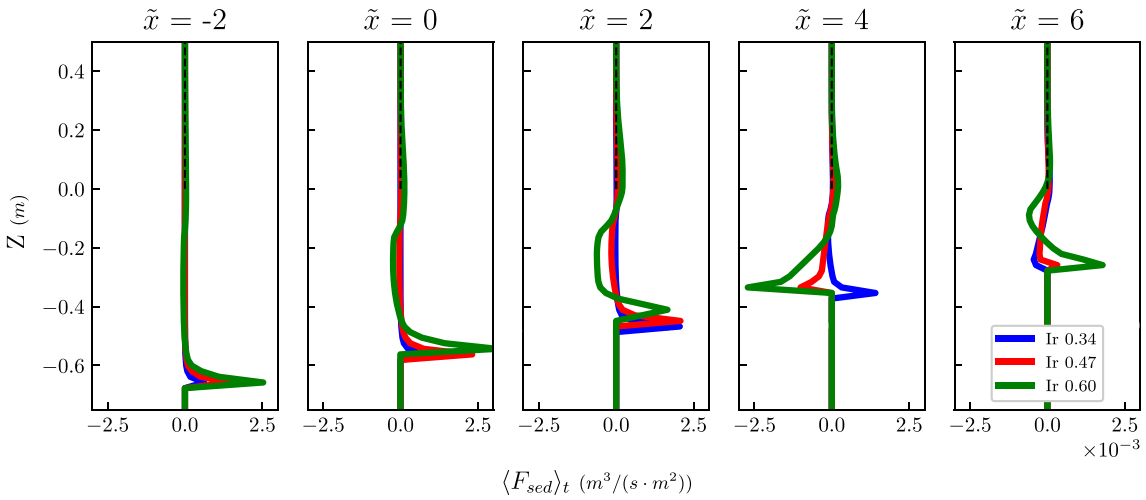

Fig. 21. Time-averaged horizontal sediment flux profiles. Obtained for waves 100 to 150.

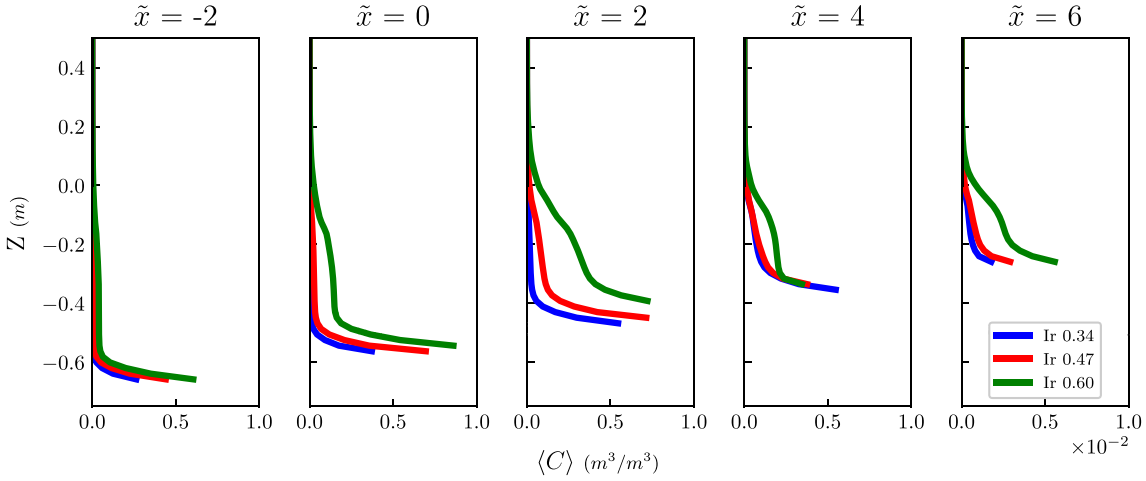

Fig. 22. Time-averaged concentration profiles for the three test cases at different positions along the beach profile. Obtained for waves 100 to 150.

3.3.3. *Suspended transport*

The suspended transport undergoes important modifications as the Iribarren number increases. As previously observed in Fig. 18, the accumulation in the outer surf zone is higher and occurs farther offshore for plunging breakers. Furthermore, the suspended contribution produces a loss of sediment at the plunge point for high Iribarren numbers, while for spilling breakers this does not occur.

In order to examine the reasons for these differences, the horizontal $\langle F_{sed,t} \rangle$ profiles are shown in Fig. 21.

The $\langle F_{sed,t} \rangle$ profiles in Fig. 21 show a clear increase in the sediment fluxes for higher Iribarren numbers, which implies that the beach profile evolves faster under plunging breakers than under spilling ones. In the shoaling zone ($\tilde{x} = -2$), the sediment flux produced by the steady streaming increases with the Iribarren number consistently with the larger wave height, which is expected to produce higher instantaneous friction velocities, stronger steady streaming and to put more sediment in suspension. In the outer surf zone ($\tilde{x} = 2$), the offshore-directed $\langle F_{sed,t} \rangle$ produced by the detached undertow is also higher for plunging breakers, which leads to a higher accumulation of sediment on the offshore face of the breaker bar and also to the higher migration speed observed in Fig. 17. This is caused by a high sediment concentration present in the upper layers of the outer surf zone. At $\tilde{x} = 4$, the undertow is still detached from the seabed in the case of spilling breakers, while for the others the undertow is attached and produces an offshore directed $\langle F_{sed,t} \rangle$, which is higher for large Iribarren numbers. As observed in Fig. 20, the $\langle U \rangle$ profile for an Iribarren number of 0.60 has a maximum close to the seabed, which is responsible for this high offshore directed $\langle F_{sed,t} \rangle$. At ($\tilde{x} = 6$), the higher Iribarren numbers produce a near-bed onshore-directed $\langle F_{sed,t} \rangle$, which is consistent with the onshore-directed $\langle U \rangle$ observed in Fig. 20. Moreover, the plunging breaker produces higher instantaneous friction velocities when the plunging jet reaches the seabed, therefore higher sediment concentrations are expected at this position. However, this near-bed onshore-directed $\langle F_{sed,t} \rangle$ is partially compensated by an offshore-directed one produced by the undertow, which depends on the amount of sediment concentration present far from the seabed, so that the net onshore-directed $\langle F_{sed,t} \rangle$ is reduced.

In addition to the previous results of $\langle U \rangle$ profiles, these patterns of the sediment flux profiles are explained based on the $\langle C \rangle$ profiles depicted in Fig. 22.

In Fig. 22, it can be noted that $\langle C \rangle$ is higher close to the seabed for larger Iribarren numbers in the shoaling zone (see $\tilde{x} = -2$), this is caused by the higher instantaneous friction velocities produced by the larger wave height (displayed in Fig. 15). Additionally, the larger accumulation of sediment in the outer surf zone for large Iribarren numbers can be related to the higher $\langle C \rangle$ in it, shown in Fig. 22 for $0 < \tilde{x} < 4$, which leads to a higher $\langle F_{sed,t} \rangle$. The reason for this is the higher instantaneous friction velocity produced by the plunging

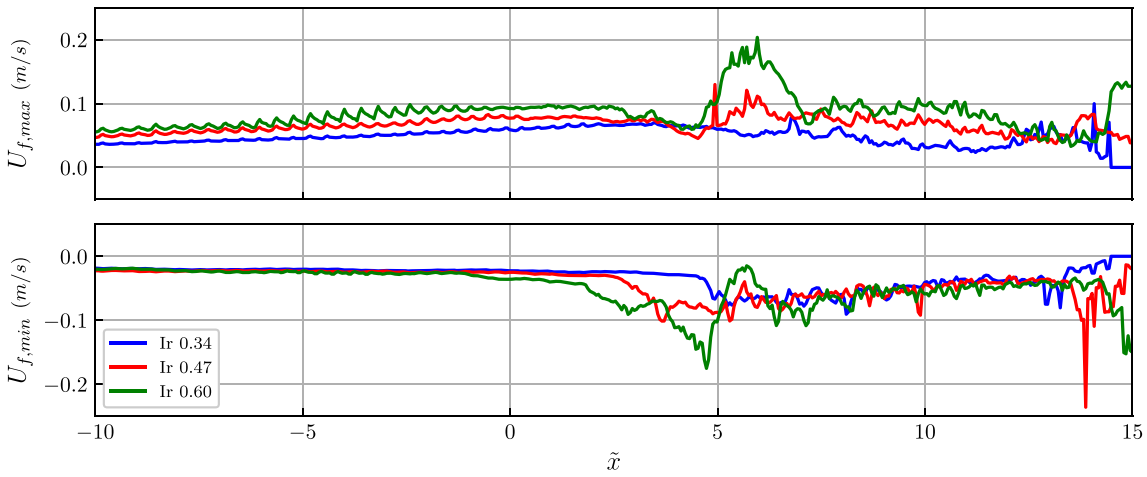

Fig. 23. Distribution of maximum and minimum friction velocity along the cross-shore profile. Obtained as the maximum value of onshore- and offshore-directed friction velocities for waves 100 to 150.

breakers in the outer surf zone, which results in a higher near-bed $\langle C \rangle$. The vertical velocities produced by the breakers advect the sediment from the lower layers to the upper ones, increasing $\langle C \rangle$ far from the seabed and enhancing the offshore directed $\langle F_{sed,t} \rangle$ of the detached undertow. Thus, more suspended sediment is transported towards the offshore face of the breaker bar. In contrast, at $\widetilde{x} = 4$ $\langle C \rangle$ is higher close to the seabed for the spilling breakers. Notice that the undertow is attached at this position for the spilling breakers while being detached for the other two test cases. This difference explains the larger $\langle C \rangle$ for the lowest Iribarren number: the concentration is advected to this position by the steady streaming. Additionally, the plunging breakers have a more uniform $\langle C \rangle$ profile at this position. This is explained by the high advection of sediment produced by the primary vortex generated in plunging breakers (named M vortex in (Sumer et al., 2013)) which distributes sediment over the water column at the breaking point. At $\widetilde{x} = 6$, $\langle C \rangle$ is much higher close to the seabed for the plunging breakers than for the other two configurations, which is consistent with the high friction velocities produced by the plunging jet where it reaches the seabed. This high near-bed $\langle C \rangle$, together with the onshore-directed $\langle U \rangle$ shown in Fig. 20, are responsible for the onshore-directed $\langle F_{sed,t} \rangle$ at the plunge point observed in Fig. 21, as explained before.

Finally, there is an interesting feature appearing for Iribarren 0.60 at $\widetilde{x} = -2$. It can be observed that there is sediment concentration in the upper layers of the shoaling zone, regardless of the absence of mixing mechanisms that could advect the sediment from the lower layers. This feature does not appear for the other two cases, and it is consistent with the sediment flux pattern proposed in this work. This concentration far from the seabed comes from the outer surf zone, advected by the detached undertow, and falls due to gravity to the lower layers as the detached undertow loses its velocity.

As commented before, one of the main sources for the differences in the accumulation rates for different types of breakers is the maximum value of the friction velocity produced by them at different positions along the cross-shore profile. To examine this, the maximum (onshore-directed) and minimum (offshore-directed) friction velocities ($U_{f,max}$ and $U_{f,min}$, respectively) produced in each of the test cases are shown in Fig. 23.

As can be observed in Fig. 23, $U_{f,max}$ of shoaling waves around the break point ($\widetilde{x} < 2.5$) is higher for the larger Iribarren numbers, which is to be expected considering their larger wave height in this zone (shown in Fig. 15). At the plunge point, $U_{f,max}$ is higher for plunging breakers than for spilling breakers (see $\widetilde{x} = 6$), which supports the previous reasoning on the origin for the onshore-directed near-bed sediment flux at this position being caused by the impinging jet; notice that the peak in $U_{f,max}$ does not occur under spilling breakers, as the impinging jet is not present. $U_{f,min}$ is larger for higher Iribarren numbers at the bar trough, which agrees with the idea of the offshore-directed flux of water exiting the outer surf zone being forced to flow close to the seabed, where the onshore-directed velocities and high mixing produced by the plunging jet are smaller. Also, for the plunging breakers, there is another peak in the $U_{f,min}$ located at the top of the breaker bar, which can be explained by the larger size of it reducing the section across which the undertow can flow. $U_{f,max}$ produced by the spilling breakers at $\widetilde{x} = 4$ are smaller than for the other cases, therefore the higher near-bed $\langle C \rangle$ observed in Fig. 22 is indeed advected by the steady streaming to this position rather than eroded at it.

Overall, plunging breakers generate higher friction velocities during the crest and trough phases, putting more sediment in suspension. This is the reason why the growth of the breaker bar occurs much faster in such a situation. In addition, the loss of sediment at the plunge point that appears under higher Iribarren number conditions is explained by the large friction velocities produced by the impinging jet, at the point where it reaches the seabed.

4. Discussion

Even if direct observation in the field or in the lab would be the most appropriate way to disentangle the complex interplay between the different processes contributing to the generation of breaker bars, the simultaneous measurement of all the different components is still a challenge. Numerical modelling based on advanced and well-tested RANS models offer, combined with the present fragmented know-how based on observations, a suitable approach to set the base for new experimental work that can help to provide a full disclosure of the mechanisms behind breaker bar generation.

4.1. Limitations of the study approach

The approach used in this study takes advantage of a newly developed numerical model which allows to access highly detailed data on the variables influencing the evolution of a cross-shore beach profile. The ability to examine morphodynamic processes with this approach is limited to the assumptions of the model.

Firstly, empirical formulae are used to avoid computing some of the sediment transport processes (i.e., bedload transport, reference concentration). This implies relying on their ability to accurately represent specific sediment transport processes. In the case of bedload transport, the choice of empirical formulae can partially affect the analysis of the bedload transport distribution, as they consider different relationships between bedload transport and friction velocity. Specifically, the

relation proposed in (Engelund and Fredsoe, 1976) results in an onshore shift of the position of the onshore face of the breaker bar respect to the undertow detachment point, as explained in Section 3.1.2. This shift adds to the one associated with wave skewness, which is addressed in Section 3.1.1. Secondly, there are limitations in terms of the simplifications in the governing equations of the model for the processes that are numerically resolved. Particularly, these affect the turbulence treatment, boundary layer approximations and the effect of alongshore features (which are not accounted for since the model is 2D). Regardless of these limitations, the model can reproduce the evolution of the beach profile and gives an overall view of how morphodynamic processes interact with each other (including those approximated by empirical formulae) to bring about the evolution of a beach profile, as demonstrated in previous validations.

Additionally, this study focuses on erosive conditions. The base case (Iribarren of 0.43) is analysed in depth, and other two erosive cases are added to verify that the different cross-shore profile evolutions are consistent with the findings of this work. In spite, most of the findings can be useful for future analysis of accretive conditions, since the underlying phenomena described in this work should be also present in milder wave conditions (although with different relative importance).

4.2. Implications of the findings

This work provides an integral view of the main drivers of cross-shore beach profile evolution, aggregating previous knowledge and new insights into the individual morphodynamic processes and establishing relationships between them. This new knowledge can be useful to better represent these processes in models suitable for simulations of larger temporal and spatial scales, resulting in improved accuracy and a reduction of the number of calibration parameters. Simpler models incorporating these aspects can be fast enough to be used in the usual design process of coastal infrastructures at larger spatial and temporal scales. Particularly, 2DV and intra-wave effects in the surf zone have been highlighted in this work as a potential source of errors in such models, and their treatment could be improved based on the new insights provided in this work. Furthermore, this knowledge can serve as a basis for future research on beach morphodynamics as the main drivers for the morphodynamic processes have been pointed.

4.3. Recommendations for future research

Further research may be aimed to validate the numerical model with experimental and field observations for a wider range of conditions (i.e., accretive) so that a similar methodology can be followed to study the morphodynamic processes under them.

The migration and equilibrium of the breaker bar have not been addressed, but the knowledge of the drivers of the cross-shore morphodynamic processes establishes a solid basis for their analysis. Researching these stages should focus on how the bathymetric changes affect the processes described in the present study, altering the accumulation patterns that they produce and resulting in a different bathymetry evolution trend.

5. Conclusions

In this work, a solid basis for the analysis of beach cross-shore morphodynamics has been provided, and the processes leading to the generation of the breaker bar have been discussed in depth. An integral analysis of the different morphodynamic processes involved in the evolution of cross-shore beach profile, analysing the contribution of each one of them, the factors that influence their contribution and how they interact with each other, has been given. Conclusions are based on the results of a numerical analysis and previous observations in experiments and field campaigns available in the literature. Additionally, a comparison between the transport rates produced by plunging and spilling breakers has been carried out.

It has been shown that the undertow detachment point plays a fundamental role in the location of the breaker bar. Its position is determined by the strength of the two fundamental near-bed currents, undertow and steady streaming, which cancel each other when time-averaged at this point. In a plane slope configuration, the undertow detachment is located in the outer surf zone, between the break and plunge points. The main drivers that can lead to changes in the undertow detachment position have been highlighted: wave skewness, wave height, mass flux produced by breaking waves, distribution of the fluid stress in the water column and water depth. Variations of these drivers, due to the bathymetric evolution or changes in wave conditions, result in a modification of the undertow detachment point and, consistently, of the accumulation patterns that produce bathymetric changes.

The bedload contribution is accountable for the generation of the onshore face of the breaker bar, on the onshore side of the undertow detachment. The shift of the position of the onshore face of the breaker bar with respect to the undertow detachment reflects the effect of wave skewness and the varying relation between bedload transport and friction velocity. The former manifests itself in the different positions of the zero-passes of U_f and U_f^3. The latter ranges from linear to cubic depending on the characteristics of the sediment and the value of the friction velocity. In the outer surf zone, and for the wave conditions of the study case, during the wave crest phase the bedload transport is a linear function of the friction velocity. In the trough phase, this relation is rather cubic. Note that the relation between bedload transport and friction velocity is treated differently in various empirical formulae.

The suspended transport contribution is responsible for the accumulation of sediment mainly on the offshore face of the breaker bar, although its accumulation zone includes almost the complete outer surf zone. The accumulation of sediment due to suspended transport on the offshore side of the undertow detachment point is produced by the sediment flux of the detached undertow, which is determined by the velocity of the detached undertow and the sediment concentration present in the upper layers of the outer surf zone.

The concentration distribution along the water depth is a consequence of the mixing mechanisms that occur in the different zones of the cross-shore profile. In the shoaling zone the weak vertical mixing is compensated by the sediment fall velocity, so that the sediment concentration is present only close to the seabed. In the outer surf zone, the upward velocities during wave breaking lift sediment form the seabed and produce more uniform concentration profiles, especially under plunging breakers. In the inner surf zone, the vortices produced in the wave breaking process induce a strong mixing of sediment along the water column.

The intra-wave effects are a consequence of the correlation between velocity and concentration, a high correlation between them leading to larger sediment fluxes. Depending on this correlation, the magnitude and, in some cases, direction of the sediment fluxes are modified with respect to those obtained directly from the time-averaged velocity and concentration. Intra-wave effects are especially noticeable close the seabed in the shoaling and outer surf zones, where they contribute to increasing the onshore-directed transport.

The comparison between accumulation rates under different types of breakers shows differences in the spatial distribution of the accumulation and loss of sediment and in the speed at which the breaker bar and trough are generated and migrate towards offshore. As the Iribarren number increases, the break, undertow detachment and plunge points are displaced offshore, and so do the resulting breaker bar and trough. Additionally, the growth and migration of the breaker bar and trough are faster in plunging breakers, as the larger instantaneous friction velocities acting on the seabed result in higher erosion and a higher amount of suspended sediment in the surf zone, making it evolve faster. Such differences are explained by the hydrodynamic and sediment transport features described in this work.

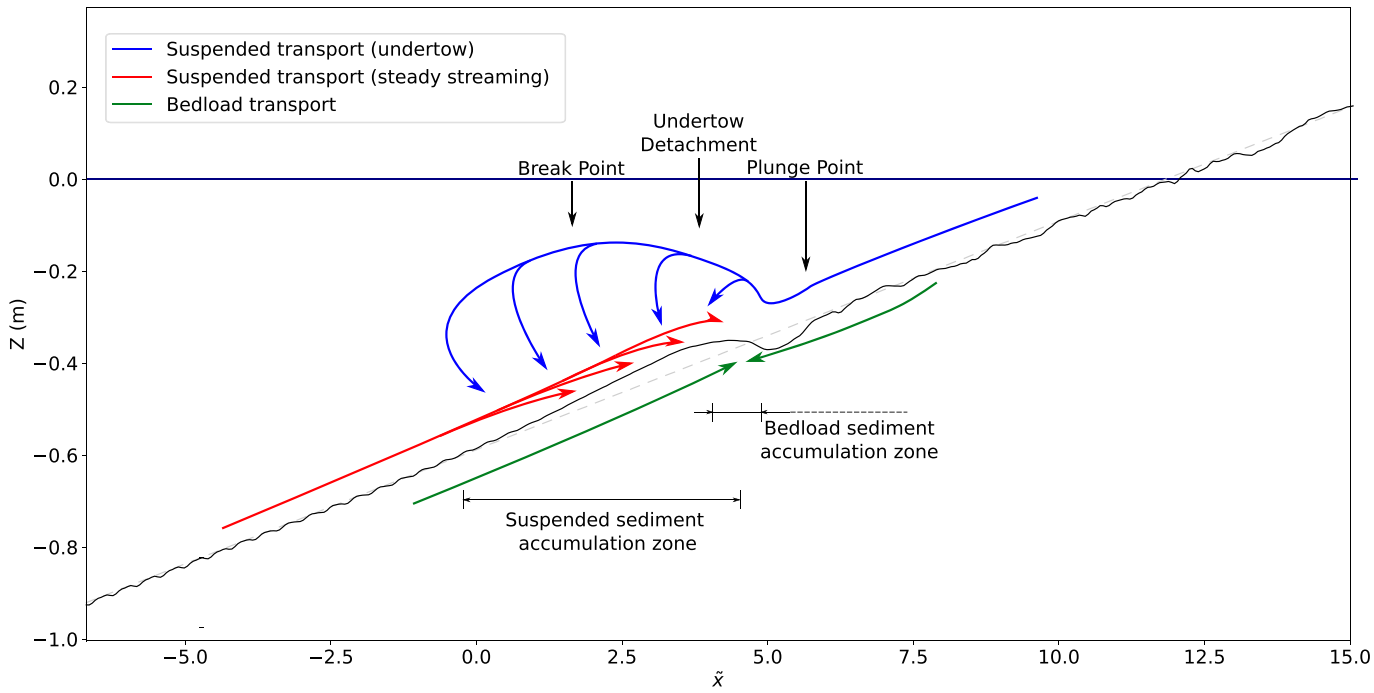

Fig. 24. Schematic description of sediment fluxes leading to the growth of the breaker bar.

Finally, the combination of the currents and sediment concentration distribution in the outer surf zone, along with the intra-wave effects, leads to a circulation of sediment in which the high vertical velocities produced during the wave breaking process lift sediment to the upper layers at the outer surf zone. This sediment is later advected by the undertow towards the shoaling zone. Due to the gravity effect, it falls into the lower layers of the shoaling zone and is carried by the steady streaming back into the outer surf zone, towards the undertow detachment. As the steady streaming is reduced offshore from the break point, part of the sediment settles leading to the accumulation responsible for the generation of the offshore face of the breaker bar.

A schematic representation of this sediment circulation pattern leading to the growth of the breaker bar is presented in Fig. 24, including the bedload and suspended transport mechanisms.

CRediT authorship contribution statement

J. García-Maribona: Conceptualization, Methodology, Software, Formal analysis, Investigation, Visualization, Writing – original draft, Writing – review & editing. **J.L. Lara:** Conceptualization, Methodology, Writing – review & editing, Funding acquisition. **M. Maza:** Conceptualization, Writing – review & editing. **I.J. Losada:** Writing – review & editing.

Declaration of competing interest

The authors declare that they have no known competing financial interests or personal relationships that could have appeared to influence the work reported in this paper.

Acknowledgements

J. García-Maribona is indebted to the MECD (Ministerio de Educación, Cultura y Deporte, Spain) for the funding provided in the FPU (Formación del Profesorado Universitario) studentship (FPU17/04356).

The work leading to this paper has been partially funded under the Retos Investigación 2018 (grant RTI2018-097014-B-I00) program of the Spanish Ministry of Science, Innovation and Universities.

References

Aagard, T., Jensen, S.G., 2013. Sediment concentration and vertical mixing under breaking waves. Mar. Geol. 336, 146–159.
Bagnold, M., 1940. Beach formation by waves: some model-experiments in a wave tank. J. Instit. Civil Eng. 15 (1), 27–52.
Bailard, J.A., Inman, D.L., 1981. An energetics bedload model for a plane sloping beach: local transport. J. Geophys. Res. 86 (C3), 2035–2043.
Baldock, T.E., et al., 2011. Large-scale experiments on beach profile evolution and surf and swash zone sediment transport induced by long waves, wave groups and random waves. Coast. Eng. 58 (2), 214–227.
Blondeaux, P., et al., 2012. Steady streaming and sediment transport at the bottom of sea waves. J. Fluid Mech. 697, 115–149.
Bruun, P., 1954. Coast Erosion and the Development of Beach Profiles. US Beach Erosion Board.
Caceres, I., Alsina, J.M., 2016. Suspended sediment transport and beach dynamics induced by monocromatic conditions, long waves and wave groups. Coast. Eng. 108, 36–55.
Dean, R., 1977. Equilibrium Beach Profiles: US Atlantic and Gulf Coasts. Department of Civil Engineering and College of Marine Studies.
Deigaard, R., Justesen, P., Fredsoe, J., 1991. Modelling of undertow by a one-equation turbulence model. Coast. Eng. 15 (5–6), 431–458.
Dubarbier, B., Castelle, B., Marieu, V., Ruessink, G., 2015. Process-based modeling of cross-shore sandbar behavior. Coast. Eng. 95, 35–50.
Engelund, F., Fredsoe, J., 1976. A sediment transport model for straight alluvial channels. Nord. Hydrol 7 (5), 293–306.
Fredsoe, J., Deigaard, R., 1992. Mechanics of Coastal Sediment Transport. s.l. World Scientific.
Gallagher, E., Elgar, S., Guza, R., 1998. Observations of sand bar evolution on a natural beach. J. Geophys. Res. 103 (C2), 3203–3216.
Garcez Faria, A.F., Thornton, E.B., Lippmann, T.C., Stanton, T.P., 2000. Undertow over a barred beach. J. Geophys. Res. 105 (C7), 16999–17010.
García-Maribona, J., Lara, J.L., Maza, M., Losada, I.J., 2021. An efficient RANS numerical model for cross-shore beach processes. Coast. Eng. 170, 103975.
Henderson, S.M., Allen, J.S., Newberger, P.A., 2004. Nearshore sandbar migration predicted by an eddy-diffusive boundary layer model. J. Geophys. Res.: Oceans 109 (C6).
Hoefel, F., Elgar, S., 2003. Wave-induced sediment transport and sandbar migration. Science 299 (5614), 1885-1885.
Holmedal, L.E., Myrhaug, D., 2009. Wave-induced steady streaming, mass transport and net sediment transport in rough turbulent ocean bottom boundary layers. Continent. Shelf Res. 29 (7), 911–926.
Kalligeris, N., et al., 2020. Calibration and assessment of process-based numerical models for beach profile evolution in southern California. Coast. Eng. 158, 103650.
Kranenburg, W.M., Ribberink, J.S., Schretlen, J.J.L.M., Uittenbogaard, R.E., 2013. Sand transport beneath waves: the role of progressive wave streaming and other free surface effects. J. Geophys. Res.: Earth Surf. 118 (1), 122–139.
Lara, J.L., Garcia, N., Losada, I.J., 2006. RANS modelling applied to random wave interaction with submerged permeable structures. Coast. Eng. 53 (5–6), 395–417.

Larsen, B.E., van der A, D.A., van der Zanden, J., Ruessink, G.F.D.R., 2020. Stabilized RANS simulation of surf zone kinematics and boundary layer processes beneath large-scale plunging waves over a breaker bar. Ocean Model. 155, 101705.
Longuet-Higgins, M.S., 1983. Wave set-up, percolation and undertow in the surf zone. Proc. Roy. Soc. Lond. Math. Phys. Sci. 390 (1799), 283–291.
Longuet-Higgins, M.S., Stoneley, R., 1953. Mass transport in water waves. Phil. Trans. Roy. Soc. Lond. Math. Phys. Sci. 245 (903), 535–581.
Lubin, P., Vincent, S., Abadie, S., Caltagirone, J.P., 2006. Three-dimensional large eddy simulation of air entrainment under plunging breaking waves. Coast. Eng. 53 (8), 631–655.
Meyer-Peter, E., Müller, R., 1948. Formulas for Bed-Load Transport. Proceedings of the 2nd Meeting of the International Association for Hydraulic Structures Research, pp. 39–64.
Nielsen, P., Svendsen, I.A., Staub, C., 1978. Onshore-offshore sediment movement on a beach. Coast. Eng. Proceed. 1 (16), 87.
Ogston, A.S., Sternberg, R.W., 2002. Effect of wave breaking on sediment eddy diffusivity, suspended-sediment and longshore sediment flux profiles in the surf zone. Continent. Shelf Res. 22 (4), 633–655.
Okayasu, A., Shibayama, T., Mimura, N., 1986. Velocity field under plunging waves. Coast. Eng. Proceed. 1 (20), 50.
Otsuka, J., Saruwatari, A., Watanabe, Y., 2017. Vortex-induced suspension of sediment in the surf zone. Adv. Water Resour. 110, 59–76.
Rattanapitikon, W., Shibayama, T., 2000. Simple model for undertow profile. Coast Eng. J. 42 (1), 1–30.
Roulund, A., Sumer, B.M., Fredsoe, J., Michelsen, J., 2005. Numerical and experimental investigation of flow and scour around a circular pile. J. Fluid Mech. 534, 351–401.
Ruessink, B.G., et al., 2011. Observations of velocities, sand concentrations and fluxes under velocity-asymmetric oscillatory flows. *J. Geophys. Res.: Oceans,* Issue C3 116.
Ruessink, B.G., Pape, L., Turner, I., 2009. Daily to interannual cross-shore sandbar migration: observations from a multiple sandbar system. Continent. Shelf Res. 29 (14), 1663–1677.
Ruffini, G., et al., 2020. Numerical modeling of flow and bed evolution of bichromatic wave groups on an intermediate beach using nonhydrostatic XBeach. J. Waterw. Port, Coast. Ocean Eng. 146 (1), 04019034.
Smith, J.D., McLean, S.R., 1977. Spatially averaged flow over a wavy surface. J. Geophys. Res. 8 (12).
Stive, M., 1986. A model for cross-shore sediment transport. Coast. Eng. Proceed. 1 (20), 114.
Sumer, B.M., et al., 2013. Laboratory observations of flow and sediment transport induced by plunging regular waves. J. Geophys. Res.: Oceans 118 (11), 6161–6182.
Svendsen, I.A., 1984. Mass flux and undertow in a surf zone. Coast. Eng. 8 (4), 347–365.
Svendsen, I.A., 2006. Introduction to Nearshore Hydrodynamics s.l.:s.n.
Tajima, Y., Madsen, O.L., 2006. Modeling near-shore waves, surface rollers, and undertow velocity profiles. J. Waterw. Port, Coast. Ocean Eng. 132 (6).
Ting, F.C.K., Kirby, J.T., 1994. Observation of undertow and turbulence in a laboratory surf zone. Coast. Eng. 24 (1), 51–80.
Ting, F.C.K., Kirby, J.T., 1995. Dynamics of surf-zone turbulence in a strong plunging breaker. Coast. Eng. 24 (3), 177–204.
Ting, F.C.K., Nelson, J.R., 2011. Laboratory measurements of large-scale near-bed turbulent flow structures under spilling regular waves. Coast. Eng. 58 (2), 151–172.
Torres-Freyermuth, A., Losada, I.J., Lara, J.L., 2007. Modeling of surf zone processes on a natural beach using Reynolds-Averaged Navier-Stokes equations. J. Geophys. Res.: Oceans 112 (C9).
van der A, D.A., et al., 2017. Large-scale laboratory study of breaking wave hydrodynamics over a fixed bar. J. Geophys. Res.: Oceans 122 (4), 3287–3310.
van der Zanden, J., et al., 2017a. Bedload and suspended load contributions to breaker bar morphodynamics. Coast. Eng. 129 (April), 72–92.
van der Zanden, J., et al., 2017b. Suspended sediment transport around a large-scale laboratory breaker bar. Coast. Eng. 125, 51–69.
van Rijn, L., Ribberink, J., van der Werf, J., Walstra, D.J., 2013. Coastal sediment dynamics: recent advances and future research needs. J. Hydraul. Res. 51 (5), 475–493.
Walstra, D., 2016. On the Anatomy of Nearshore Sandbars.
Wang, P., Ebersole, B.A., Smith, E.R., 2003. Beach-profile evolution under spilling and plunging breakers. J. Waterw. Port, Coast. Ocean Eng. 129, 41–46.
Wang, P., Smith, E.R., Ebersole, B.A., 2002. Large-scale laboratory measurements of longshore sediment transport under spilling and plunging breakers. J. Coast Res. 18 (1), 118–135.